ARTICLE

https://doi.org/10.1038/s41586-019-1563-y

Electrical and synaptic integration of glioma into neural circuits

Humsa S. Venkatesh[1], Wade Morishita[2,3], Anna C. Geraghty[1], Dana Silverbush[4,5,6], Shawn M. Gillespie[1], Marlene Arzt[1], Lydia T. Tam[1], Cedric Espenel[7], Anitha Ponnuswami[1], Lijun Ni[1], Pamelyn J. Woo[1], Kathryn R. Taylor[1], Amit Agarwal[8,15], Aviv Regev[5,6,9], David Brang[10], Hannes Vogel[1,11,12], Shawn Hervey-Jumper[13], Dwight E. Bergles[8], Mario L. Suvà[4,5,6], Robert C. Malenka[2,3] & Michelle Monje[1,2,11,12,14]*

High-grade gliomas are lethal brain cancers whose progression is robustly regulated by neuronal activity. Activity-regulated release of growth factors promotes glioma growth, but this alone is insufficient to explain the effect that neuronal activity exerts on glioma progression. Here we show that neuron and glioma interactions include electrochemical communication through bona fide AMPA receptor-dependent neuron–glioma synapses. Neuronal activity also evokes non-synaptic activity-dependent potassium currents that are amplified by gap junction-mediated tumour interconnections, forming an electrically coupled network. Depolarization of glioma membranes assessed by in vivo optogenetics promotes proliferation, whereas pharmacologically or genetically blocking electrochemical signalling inhibits the growth of glioma xenografts and extends mouse survival. Emphasizing the positive feedback mechanisms by which gliomas increase neuronal excitability and thus activity-regulated glioma growth, human intraoperative electrocorticography demonstrates increased cortical excitability in the glioma-infiltrated brain. Together, these findings indicate that synaptic and electrical integration into neural circuits promotes glioma progression.

High-grade gliomas are the leading cause of central nervous system cancer-related death in both children and adults. This clinical intractability indicates that the current understanding of glioma pathophysiology is insufficient. Gliomas infiltrate extensively within the brain and spinal cord, but growth outside the central nervous system is exceedingly rare. Glioma progression is regulated not only by cell-intrinsic mechanisms, but also by important microenvironmental dependencies. Neurons are a crucial component of the glioma microenvironment and regulate malignant growth in an activity-dependent manner[1,2]. Activity-regulated release of neuroligin-3 (NLGN3)[1,2] is required for glioma progression[2], indicating a fundamental role in glioma pathophysiology that is incompletely explained by stimulation of classical oncogenic signalling pathways alone[2]. We previously found that NLGN3 induces glioma expression of numerous synaptic genes[2], raising the possibility that glioma may engage in synaptic communication. Synapses exist between neurons and normal oligodendroglial precursor cells (OPCs)[3,4], and electrochemical signalling can regulate the proliferation, differentiation or survival of OPCs and of other neural precursor cells[5–9]. As cellular subpopulations within gliomas closely resemble OPCs[10,11], we proposed that gliomas may also engage in synaptic communication and that this integration into neural circuits may be fundamental to glioma progression.

Synaptic gene expression in glioma

To examine synaptic gene expression in primary human glioma, we analysed single-cell transcriptomic datasets generated from pre-treatment biopsy samples of the major classes of adult and paediatric high-grade gliomas, including adult isocitrate dehydrogenase (IDH)-mutant glioma[11], adult IDH wild-type glioma[10], and paediatric histone-H3 mutant (H3K27M) diffuse midline glioma (DMG; pontine DMG is also known as diffuse intrinsic pontine glioma (DIPG))[10]. We found broad expression of glutamate receptor genes and postsynaptic structural genes in malignant glioma cells (Fig. 1a, Extended Data Fig. 1a). Unsupervised principal component analysis revealed enrichment of synaptic gene expression within distinct malignant cellular subpopulations (Fig. 1b). Gliomas consist of cellular subpopulations that resemble various stages of astrocytic and oligodendrocytic differentiation[10,11]. Synaptic gene enrichment was mainly found in glioma cells that resemble OPCs (Fig. 1b, Extended Data Fig. 2c)—a glial cell type that normally functions as a postsynaptic cell[3,4]. These observations are consistent with the principle that malignant cellular subpopulations assume distinct roles in the heterogeneous cancer ecosystem. Concordant with these findings from primary biopsy tissue (Fig. 1b), single-cell transcriptomics of patient-derived H3K27M$^+$ glioma xenografts demonstrated synaptic gene enrichment in the OPC-like subpopulation (Extended Data Figs. 1b, 2a, b).

Neuron–to–glioma synapses

Having established that primary glioma cells express a repertoire of synaptic genes, we next assessed whether structural synapses form between glioma cells and neurons in the tumour microenvironment. Examination of primary glioblastoma tissue ultrastructure using electron microscopy revealed clear synaptic structures (Extended Data Fig. 2d). To confirm that glioma cells participate in such putative

[1]Department of Neurology, Stanford University, Stanford, CA, USA. [2]Department of Psychiatry and Behavioral Sciences, Stanford University, Stanford, CA, USA. [3]Nancy Pritzker Laboratory, Stanford University, Stanford, CA, USA. [4]Department of Pathology and Center for Cancer Research, Massachusetts General Hospital and Harvard Medical School, Boston, MA, USA. [5]Klarman Cell Observatory, Broad Institute of Harvard and MIT, Cambridge, MA, USA. [6]Broad Institute of Harvard and MIT, Cambridge, MA, USA. [7]Cell Sciences Imaging Facility, Stanford University School of Medicine, Stanford, CA, USA. [8]Department of Neuroscience, Johns Hopkins University, Baltimore, MA, USA. [9]Howard Hughes Medical Institute, Koch Institute for Integrative Cancer Research, Department of Biology, MIT, Cambridge, MA, USA. [10]Department of Psychology, University of Michigan, Ann Arbor, MI, USA. [11]Department of Pathology, Stanford University, Stanford, CA, USA. [12]Department of Pediatrics, Stanford University, Stanford, CA, USA. [13]Department of Neurological Surgery, University of California, San Francisco, San Francisco, CA, USA. [14]Institute for Stem Cell Biology and Regenerative Medicine, Stanford University, Stanford, CA, USA. [15]Present address: The Chica and Heinz Schaller Research Group, Institute for Anatomy and Cell Biology, Heidelberg University, Heidelberg, Germany. *e-mail: mmonje@stanford.edu

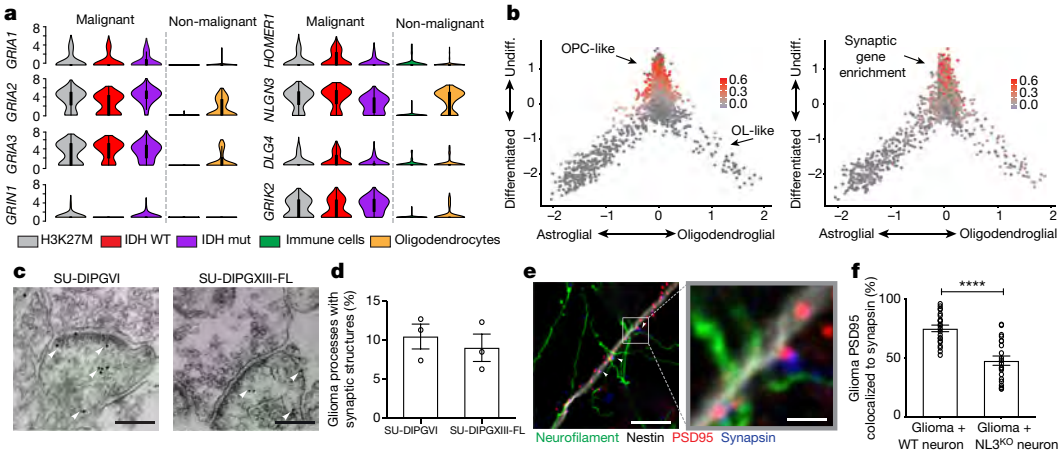

Fig. 1 | Transcriptomic and structural evidence for glioma synapses. **a**, Primary human biopsy single-cell transcriptomic data illustrating synapse-associated gene expression levels from H3K27M$^+$ DMG (grey; $n = 2{,}259$ cells, 6 study participants), IDH wild-type (WT) adult high-grade glioma (red; $n = 599$ cells, 3 participants), IDH mutant (mut) adult high-grade glioma (purple; $n = 5{,}096$ cells, 10 participants) malignant cells, and tumour-associated, non-malignant immune cells (green; $n = 96$ cells, 5 participants) and oligodendrocytes (yellow; $n = 232$ cells). For each individual violin plot, the y axis represents $\log_2$(transcripts per million); the x axis represents the number of individual cells with indicated expression value; and thick and thin black lines represent interquartile and 1.5× interquartile range, respectively. **b**, Plot of the lineage (x axis) and stemness (undifferentiated to differentiated; y axis) scores for H3K27M$^+$ DMG malignant single cells sorted from primary biopsies ($n = 2{,}259$ cells). Overlay of grey-red enrichment score indicates relative score for OPC-like genes (left) and synapse-related genes (right; Pearson correlation rho = 0.47, $P < 0.0001$). OL, oligodendrocyte. **c**, Immuno-electron microscopy of patient-derived DIPG cells SU-DIPG-VI (left) and SU-DIPG-XIII-FL (right; FL denotes frontal lobe tumour) xenografted into the mouse hippocampus. Arrowheads denote immuno-gold particle labelling of GFP. Postsynaptic density in GFP$^+$ tumour cells (pseudo-coloured green), synaptic cleft, and clustered synaptic vesicles in apposing presynaptic neuron (pseudo-coloured magenta) identify synapses. Scale bars, 200 μm. **d**, Quantification of neuron–glioma synaptic structures in SU-DIPG-VI and SU-DIPG-XIII-FL xenografts expressed as a percentage of total identified glioma cell processes that form unambiguous synaptic structures ($n = 3$ mice per group). **e**, Representative confocal image of neurons co-cultured with PSD95–RFP-labelled glioma cells. White box and arrowheads highlight region of synaptic puncta colocalization; magnified view is shown to the right. Green denotes neurofilament (axon); white denotes nestin staining (glioma cell processes); blue denotes synapsin (presynaptic puncta); red denotes PSD95–RFP staining (postsynaptic puncta). Scale bars, 10 μm (left) and 2 μm (right). **f**, Quantification of the colocalization of postsynaptic glioma-derived PSD95–RFP with neuronal presynaptic synapsin in co-cultures of glioma cells (SU-DIPG-VI) with wild-type ($n = 22$ cells, 10 coverslips) or *Nlgn3*^{KO} (NL3^{KO}; $n = 21$ cells, 10 coverslips) neurons. Data are mean ± s.e.m. (**d**, **f**). ****$P < 0.0001$, two-tailed Student's t-test.

neuron–glioma synapses, we performed immuno-electron microscopy in green fluorescent protein (GFP)-labelled, patient-derived glioma xenografts. Immuno-electron microscopy analyses unambiguously identified GFP$^+$ glioma cells on the postsynaptic side of synaptic structures, with synapses on approximately 10% of GFP$^+$ glioma processes (Fig. 1c, d, Extended Data Fig. 2e–g). To test the contribution of microenvironmental NLGN3 to neuron–glioma synaptogenesis, we next co-cultured glioma cells expressing fluorescently tagged postsynaptic density protein-95 (PSD95) with wild-type or *Nlgn3*-knockout (*Nlgn3*^{KO}) neurons. We found a marked reduction in the co-localization of neuronal presynaptic puncta (synapsin) with glioma postsynaptic puncta (PSD95–RFP) in co-cultures with *Nlgn3*^{KO} neurons compared with wild-type neurons (Fig. 1e, f, Extended Data Fig. 2h). This further implicates NLGN3 in the formation of neuron-glioma synapses—a function distinct from its role in stimulating classical oncogenic signalling pathways (Extended Data Fig. 3a–c).

Focusing on paediatric gliomas, we next tested whether neurons and glioma cells establish electrophysiologically functional synapses using four distinct patient-derived orthotopic xenograft models (Extended Data Table 1). GFP-labelled glioma cells were stereotactically xenografted into the CA1 region of the hippocampal circuit. After a period of engraftment and growth, acute hippocampal slices were prepared for whole-cell patch-clamp recordings of GFP$^+$ glioma cells. Stimulation of Schaffer collateral and commissural afferent axons that arise from the CA3 region while patch-clamping glioma cells from the CA1 region enables measurement of the glioma response to axonal activity (Fig. 2a, b). Voltage-clamp recordings revealed stimulation-evoked fast (<5 ms) inward currents consistent with excitatory postsynaptic currents (EPSCs; Fig. 2c). Current-clamp recordings demonstrated that these inward currents were depolarizing (Fig. 2d). Glioma EPSCs were blocked by the voltage-gated sodium channel blocker tetrodotoxin (TTX; Fig. 2e), illustrating dependence on neuronal action potentials.

Measurement of the current–voltage relationship (I–V curve) illustrated reversal at approximately 0 mV (Fig. 2f) and glioma EPSCs displayed facilitation in response to paired stimuli (Fig. 2g), both of which are electrophysiological characteristics that suggest that synaptic communication occurs through AMPA (α-amino-3-hydroxy-5-methyl-4-isoxazole propionic acid) receptors (AMPARs; a type of ionotropic glutamate receptor). Concordantly, glioma EPSCs were blocked by the AMPAR antagonist NBQX (2,3-dihydroxy-6-nitro-7-sulfamoyl-benzo[f]quinoxaline; Fig. 2g–i) and decreased by the calcium-permeable AMPAR antagonist NASPM (1-naphthyl acetyl spermine; Extended Data Fig. 3d, e). AMPARs that lack the GluA2 subunit, or that contain GluA2 that has not undergone RNA editing of its glutamine/arginine (Q/R) site, are calcium-permable[12,13]. GluA2 is broadly expressed in gliomas (Fig. 1a); examination of RNA editing of the Q/R site in paediatric glioma demonstrated GluA2 under-editing (approximately 50–70% edited; Extended Data Fig. 3f, g). Together, these results indicate that axon stimulation-evoked, millisecond timescale glioma cell currents require action potentials and are mediated by AMPARs—properties consistent with the conclusion that subpopulations of glioma cells form bona fide synapses with neurons. This conclusion is also supported by the evidence for neuron-to-glioma synapses described in a companion paper[14].

To test this hypothesis further, we replaced extracellular calcium with strontium, a manipulation that facilitates the release of asynchronous presynaptic vesicles[15] (Fig. 2j). In the presence of strontium we detected small, fast inward currents consistent with miniature EPSCs, indicating quantal responses to synaptic vesicles[15] in glioma cells. Quantal glioma miniature EPSCs were similarly blocked by NBQX (Fig. 2j). No fast, large currents indicative of action potentials were observed in any of the more than 640 glioma cell recordings. Together, these results indicate that synaptic transmission occurs between glutamatergic neurons and a subset of xenografted human

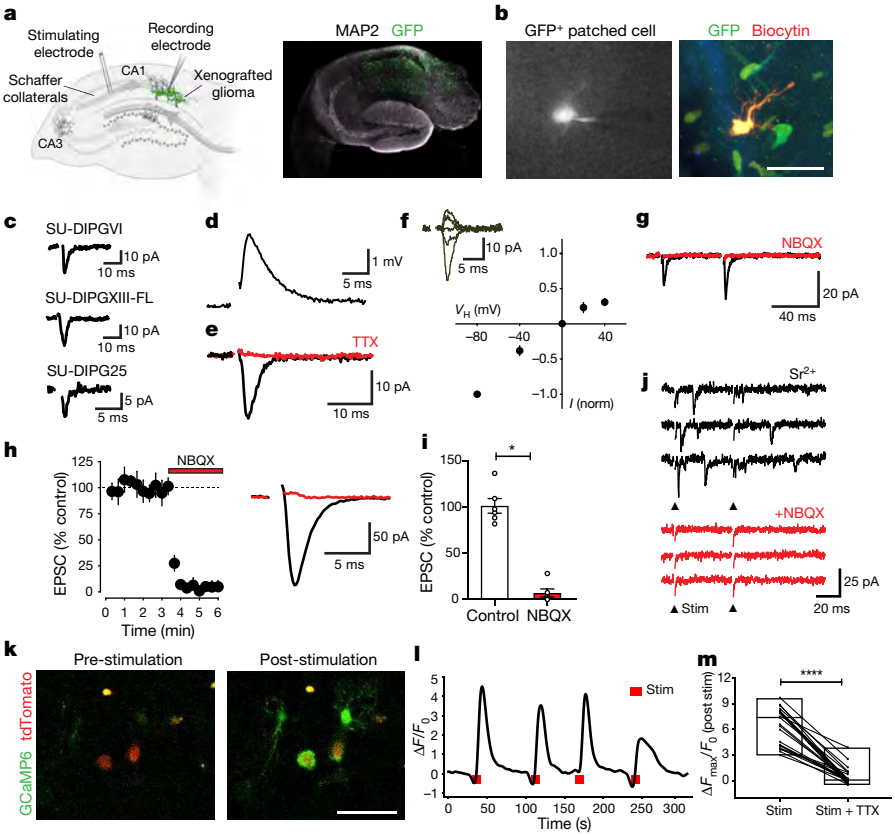

Fig. 2 | Synaptic AMPAR-mediated EPSCs in glioma. a, Left, electrophysiological model. GFP$^+$ glioma cells (green) xenografted in mouse hippocampus CA1 region with Schaffer collateral afferent stimulation. Right, representative hippocampal slice micrograph (tiled image taken with 10× objective); $n = 8$ biological replicates. Green denotes GFP$^+$ glioma cells; white denotes MAP2 staining (neuronal cells). **b**, Left, representative micrograph of patched GFP$^+$ glioma cell with whole-cell pipette containing biocytin dye. Right, biocytin (red)-filled glioma cell co-labelled with GFP (green). Scale bar, 50 μm; $n = 21$ biological replicates. **c**, Representative traces of evoked EPSCs in patient-derived glioma xenografts. **d**, Representative glioma excitatory postsynaptic potential (EPSP) in current-clamp with Schaffer collateral stimulation. **e**, Representative evoked glioma EPSC before (black) and after (red) application of TTX (0.5 μM). **f**, Current–voltage relationship of evoked EPSCs with representative traces shown as inset (−80 mV: $n = 18$ cells, 9 mice; −40 mV: $n = 5$ cells, 2 mice; 0 mV: $n = 18$ cells, 9 mice; +20 mV: $n = 7$ cells, 2 mice; +40 mV: $n = 16$ cells, 7 mice). **g**, Paired-pulse facilitation of evoked glioma cell EPSCs (black) with block by 10 μM NBQX (red; 50 ms inter-stimulus interval: $P_2/P_1 = 1.75 \pm 0.12$; $n = 8$ cells, 8 mice). **h**, Left, time course of evoked glioma cell EPSC block by 10 μM NBQX (red bar denotes duration; $n = 6$ cells, 6 mice). Right, representative trace before (black) and after (red) application of NBQX. **i**, Quantification of data in **h**. **j**, Evoked miniature EPSCs in the presence of 4 mM strontium (top) and block by 10 μM NBQX (bottom) ($n = 4$ cells, 2 mice). Arrowhead denotes the stimulation time point (downward deflection in NBQX is a stimulation artefact). **k**, Two-photon in situ calcium imaging in SU-DIPG-VI xenograft with Schaffer collateral stimulation ($n = 12$ slices, 4 mice). Representative frames shown before (left) and after (right) stimulation. Red denotes glioma tdTomato nuclear tag; green denotes glioma GCaMP6s. Scale bar, 50 μm. **l**, GCaMP6s intensity trace in representative glioma cell with electrical stimulation (red bar) over time ($n = 4$ mice). Time point of stimulation is denoted by red bars. **m**, Individual cell GCaMP6s response to electrical stimulation with or without 0.5 μM TTX ($n = 26$ cells, 3 mice). Data are mean ± s.e.m. (**g**–**i**, **m**). *$P < 0.05$, ****$P < 0.0001$, one-tailed Wilcoxon matched-pairs signed rank test.

glioma cells, exhibiting properties similar to synapses formed with normal OPCs[3,4].

To explore the consequences of activity-dependent currents in glioma further, we performed in situ two-photon calcium imaging of xenografted glioma cells that express the genetically encoded calcium indicator GCaMP6s. Glioma-specific expression of the calcium indicator was validated by co-staining for human nuclear antigen (HNA; Extended Data Fig. 4a). Spontaneous calcium transients were consistently observed (Extended Data Fig. 4b–d). Stimulation of Schaffer collateral and commissural afferents elicited calcium transients in glioma cells located in the CA1 target area of the stimulated axons (Fig. 2k, l), which provides additional evidence that endogenous circuit activity may exert functionally relevant effects on glioma cells. These evoked calcium transients were blocked by tetrodotoxin (TTX; Fig. 2m, Extended Data Fig. 4e).

Activity-dependent potassium currents

A longer duration electrophysiological response to neuronal activity was found in a subset of glioma cells (Fig. 3a). Distinct from the classical EPSCs (<5 ms) described earlier, these prolonged currents (>1 s) exhibited kinetics that are inconsistent with a synaptic response and are instead reminiscent of the neuronal activity-evoked currents observed in normal astrocytes. Supporting the idea that these prolonged currents are distinct from the synaptic responses described earlier, the calcium-permeable AMPAR inhibitor NASPM had no effect (Extended Data Fig. 5a, b). These prolonged glioma currents were blocked by TTX (Fig. 3b, c). In further support of a response coupled to neuronal population firing, the morphology of the prolonged currents revealed spike-like waveforms phase-locked to neuronal field potential waveforms that scaled with increased axonal stimulation intensity (Extended Data Fig. 5c, d). Simultaneous whole-cell current-clamp and field potential recordings reveal that the prolonged current amplitude scaled directly with field potential, meaning that prolonged glioma current amplitude increases with increasing neuronal activity (Extended Data Fig. 5e, f). In normal astrocytes, activity-dependent currents are attributable to glutamate transporter currents and inward potassium currents that occur with a rise in extracellular potassium from neurons[16–18]. Consistent with a direct role for increases in extracellular

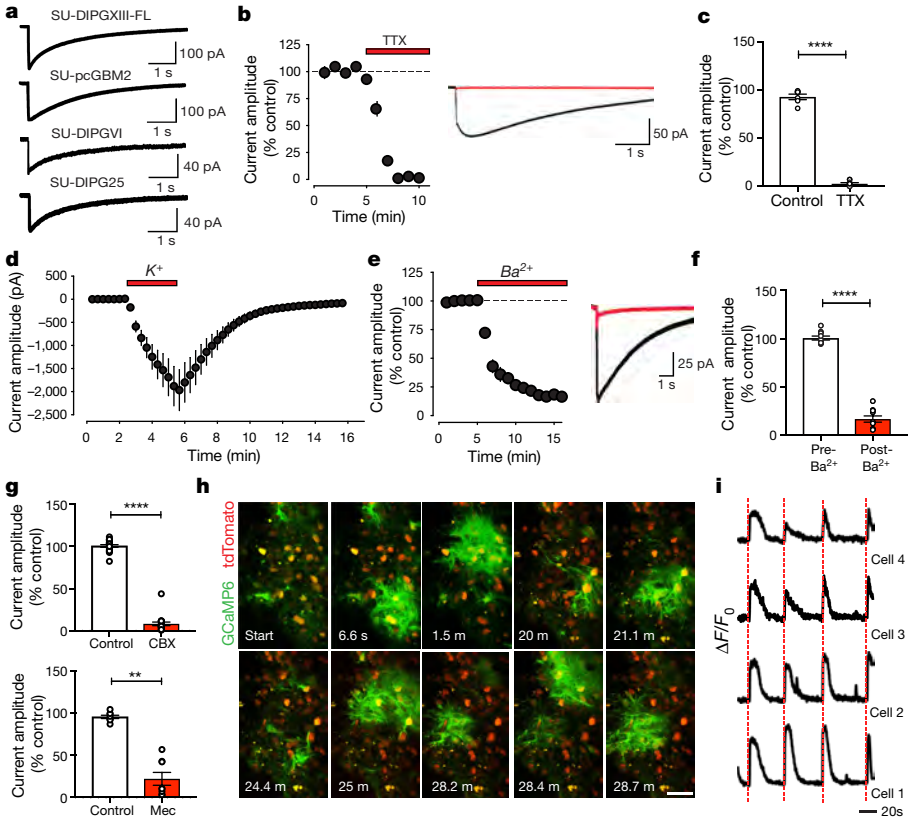

Fig. 3 | Neuronal activity-dependent potassium currents in glioma. **a**, Representative voltage-clamp traces of evoked prolonged current in several patient-derived glioma xenograft models. **b**, Left, time course of evoked current blocked by TTX (red bar denotes duration; $n = 6$ cells, 6 mice). Right, representative trace before (black) and after (red) TTX (right). **c**, Quantification of data in **b**. **d**, Time course of glioma cell current induced by addition of extracellular potassium (15 mM K^+; red bar denotes duration; $n = 9$ cells, 2 mice) with concurrent neuronal activation blockade. **e**, As in **b**, but with 200 μM barium ($n = 10$ cells, 3 mice). **f**, Quantification of data in **e**. **g**, Quantification of current amplitude decrease with 100 μM CBX ($n = 19$ cells, 11 mice; top), or 100 μM meclofenamate (Mec; $n = 8$ cells, 3 mice; bottom). **h**, Two-photon in situ calcium imaging of hippocampal slice xenografted with GCaMP6s-expressing glioma (SU-DIPG-XIII-FL); 30-min (m) time course without axonal stimulation ($n = 27$ slices, 14 mice). Red denotes glioma tdTomato nuclear tag; green denotes glioma GCaMP6s. Scale bar, 50 μm. **i**, Phase-locked traces of GCaMP6s intensity over time in four synchronous glioma cells with axonal stimulation (red line; $n = 40$ cells, 4 mice). Data are mean ± s.e.m. (**b**–**g**). $^{**}P < 0.01$, $^{****}P < 0.0001$, two-tailed paired Student's *t*-test (**c**, **f**), or one-tailed Wilcoxon matched-pairs signed rank test (**g**).

potassium in generating these prolonged currents, large prolonged glioma currents were elicited by application of potassium alone with neuronal activity pharmacologically blocked (Fig. 3d, Extended Data Fig. 5g). Furthermore, activity-dependent prolonged currents were largely diminished by barium, an ion that blocks inwardly rectifying potassium channels (Fig. 3e, f). By contrast, application of the glutamate transporter antagonist dl -threo-β-benzyloxyaspartate (TBOA) had a negligible effect (Extended Data Fig. 5h). Together, these results support the interpretation that non-synaptic, prolonged glioma currents mainly reflect potassium flux attributable to a rise in extracellular potassium with neuronal activity.

Gap junction coupling amplifies currents

Glioma cells with prolonged currents exhibit markedly low input resistance (Extended Data Fig. 6a), reminiscent of astrocytes. Extensive gap junctional coupling is partially responsible for this low membrane resistance in astrocytes[19]. Gap junctions couple adult glioma cells through long processes known as tumour microtubes[20], which we also find in primary paediatric glioma tissue (Extended Data Fig. 5j–o). To determine whether glioma cells exhibiting prolonged currents are gap junction-coupled, single cells were filled with the small molecular mass biocytin dye. Subsequent confocal imaging revealed that biocytin diffused throughout a network of cells (Extended Data Fig. 6b), which supports the existence of a gap junction-coupled network. To test this conclusion, we applied the gap junction blockers carbenoxolone (CBX) or meclofenamate, which both reduced the amplitude of prolonged glioma currents (Fig. 3g, Extended Data Figs. 6c–e, h, i) while simultaneously increasing glioma input resistance (Extended Data Figs. 6f, g, j, k). Together, these observations strongly suggest that activity-regulated increases in extracellular potassium concentrations cause glioma depolarization, and a gap junction-coupled glioma network amplifies the consequences of activity-induced changes in the extracellular ionic environment.

Two-photon calcium imaging further revealed distinct synchronous network calcium transients that both occur spontaneously (Fig. 3h, Extended Data Fig. 5i, Supplementary Video 1) and are elicited by afferent stimulation (Fig. 3i, Supplementary Video 2). This synchronicity could be explained by gap junction coupling, and accordingly was blocked by the application of CBX (Extended Data Fig. 6l–o, Supplementary Video 3), further indicating a functional glioma network through which depolarizing currents propagate. Demonstration of glutamatergic chemical synapses (Fig. 2) and activity-dependent, non-synaptic potassium currents (Fig. 3) build on early work illustrating glutamate-dependent currents in glioblastoma[21] to underscore the surprising observation that this cancer is an electrically active tissue (see Supplementary Videos 1–3).

Gliomas exhibit intratumoral and intertumoral cellular heterogeneity, with subpopulations of cancer cells assuming particular roles and even very small cellular fractions proving essential for cancer progression[22]. Considering all paediatric glioma cells examined ($n = 643$), we find that approximately 5–10% of glioma cells exhibit synaptic EPSCs, and 40% of cells exhibit prolonged currents in response to neuronal activity. Although all four patient-derived xenograft models exhibited neuronal activity-evoked inward currents, the proportion of cells

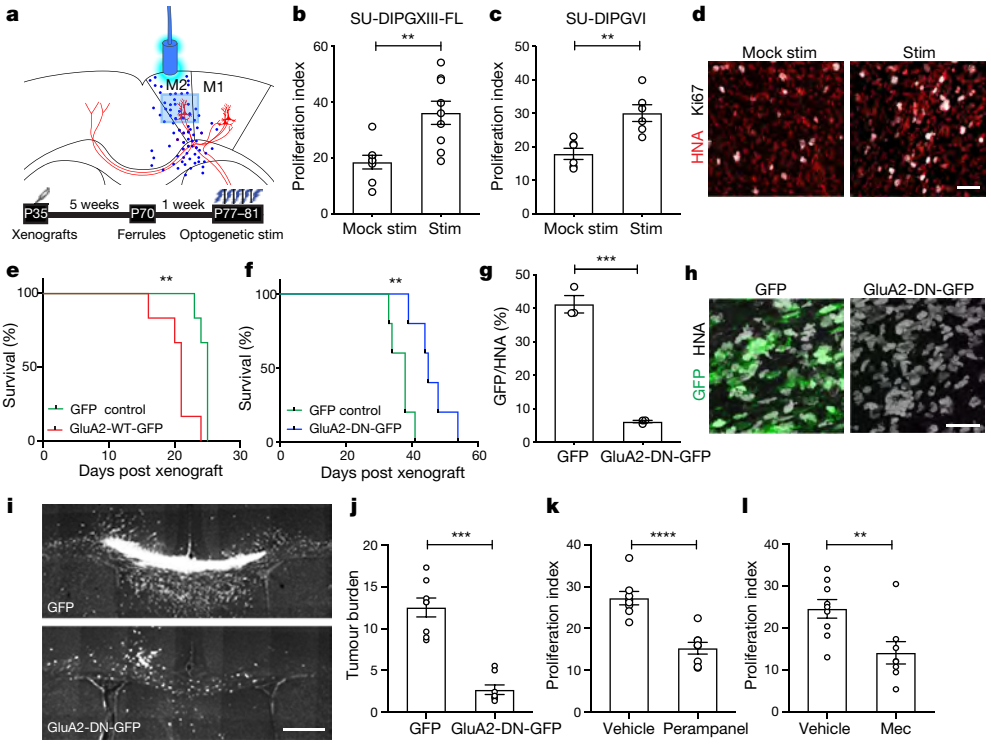

Fig. 4 | Glioma membrane depolarization promotes glioma progression. a, Optogenetic model for glioma depolarization. Blue dots represent ChR2-expressing glioma cells; light blue rectangle denotes region of analysis. P, postnatal day. **b**, Proliferation index of SU-DIPG-XIII-FL-ChR2 xenografts after mock stimulation or blue light stimulation, measured as percentage of GFP^+/HNA^+ cells expressing Ki67 (mock stim, $n = 8$; stim, $n = 9$ mice). **c**, As in **b** but for SU-DIPG-VI-ChR2 xenografts ($n = 6$ mice per group). **d**, Representative confocal micrographs from **c**, illustrating proliferation of SU-DIPG-VI-ChR2 xenografts. Red denotes human nuclei staining by HNA; white denotes Ki67. Scale bar, 50 μm. **e**, **f**, Kaplan–Meier survival curves of SU-DIPG-XIII-P* (P denotes pontine tumour) xenografts that overexpress GFP-only (green) or GluA2-WT-GFP (red) (**e**) and GFP-only (in 80% of cells, green) or GluA2-DN-GFP (in 80% of cells, blue) (**f**) ($n = 5$ mice per group). **g**, Competitive outgrowth of non-GluA2-DN-GFP-expressing cells in **f**, determined by proportion of GFP to total human nuclei (HNA) pixel intensity; ($n = 3$ mice per group). **h**, Representative confocal micrographs of experiments in **f** and **g**. White denotes human nuclei; green denotes GFP. Scale bar, 50 μm. **i**, Representative confocal images of SU-DIPG-XIII-FL xenografts that express GFP-only (top) or GluA2-DN-GFP (bottom). Grey denotes MBP (myelin basic protein staining shown to delineate brain structure); white denotes glioma-GFP. Scale bar, 500 μm. **j**, Quantification of data in **i** ($n = 8$ mice per group). **k**, Proliferation index of SU-DIPG-VI xenografts treated with the AMPAR blocker perampanel or vehicle control ($n = 8$ mice per group). **l**, Proliferation index of SU-DIPG-XIII-FL in mice treated with the gap junction blocker meclofenamate or vehicle control ($n = 9$ vehicle, $n = 8$ treated mice). Data are mean ± s.e.m. (**b**, **c**, **g**, **j**–**l**). $^{**}P < 0.01$. $^{***}P < 0.001$, $^{****}P < 0.0001$, two-tailed unpaired Student's *t*-test (**b**, **c**, **g**, **k**, **l**), two-tailed log rank analyses (**e**, **f**), or two-sided Mann–Whitney test (**j**).

that display fast EPSCs or prolonged currents varies between patient-derived models. This intertumoral heterogeneity is evident even within a molecularly defined subtype such as $H3K27M^+$ glioma and is predicted by the varied composition of OPC-like and astrocyte-like compartments in individual tumours (Extended Data Figs. 2b, 7a).

Depolarization promotes glioma proliferation

Depolarization can profoundly affect cellular behaviour[5–9], and we have found two distinct mechanisms by which neuronal activity induces glioma cell membrane depolarization. To test whether depolarization of the glioma cell membrane promotes proliferation, we used in vivo optogenetic techniques to depolarize xenografted glioma cells that express the blue light-sensitive cation channel channelrhodopsin-2 (ChR2; Extended Data Fig. 7b). Glioma cells that express ChR2–YFP were xenografted to the cortex, and after a period of engraftment and growth, blue light was delivered to depolarize the glioma xenograft in vivo. Compared with mock-stimulated control groups, we found that glioma depolarization robustly promoted glioma xenograft proliferation (Fig. 4a–d). Exposure to blue light alone had no effect on proliferation or apoptosis in control glioma xenografts (Extended Data Fig. 7c–e).

Targeting electrochemical communication

As membrane depolarization promotes glioma proliferation, we next tested the relative functional contributions of each mechanism of electrochemical communication, beginning with AMPAR-mediated EPSCs. We overexpressed the wild-type GluA2 subunit fused to GFP, GFP alone, or a dominant-negative GluA2 (GluA2-DN-GFP) in glioma and confirmed decreased conductance in GluA2-DN-GFP-expressing glioma cells (Extended Data Fig. 7f, g). Mice bearing xenografts that overexpress wild-type GluA2–GFP survived a shorter time than GFP-only xenografts, whereas mice bearing GluA2-DN-GFP xenografts exhibited improved survival and decreased tumour burden compared with GFP-only controls (Fig. 4e–j, Extended Data Fig. 8a, b). To test for a possible in vivo growth advantage of GluA2 expression, we xenografted a mixture of 80% GluA2-DN-GFP construct-expressing and 20% non-expressing cells and found that tumours were composed almost entirely of non-GluA2-DN-GFP-expressing cells at the survival endpoint (Fig. 4g, h).

Similar to in vivo experiments, co-cultures of glioma cells with neurons markedly increased proliferation. NBQX partially reduced this effect (Extended Data Fig. 8c, d); neuronal-secreted factors such as NLGN3 account for residual increased levels of proliferation[1]. Given the stark effect of AMPAR function on glioma growth in vivo and in co-culture, we next tested the relative contributions of cell-intrinsic glutamate signalling mechanisms. Although paracrine or autocrine AMPAR signalling may promote adult glioblastoma growth[23,24], NBQX had no effect on paediatric glioma proliferation in the absence of neurons (Extended Data Fig. 8c, d). Testing cell-intrinsic effects of GluA2-DN expression, we also found no difference in growth rate or

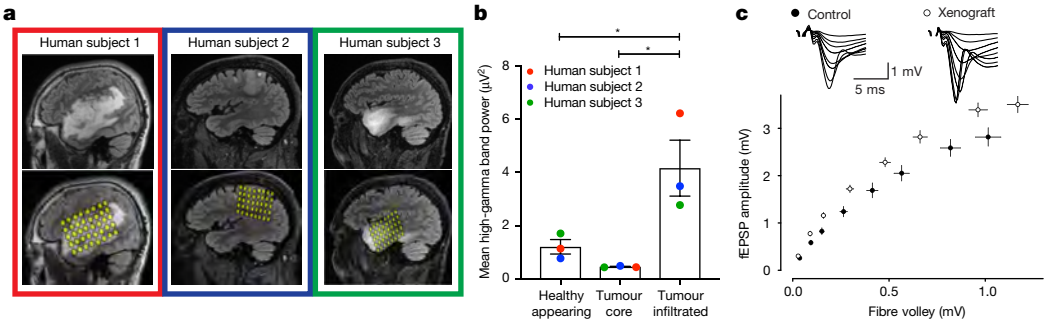

Fig. 5 | Increased neuronal excitability in glioma-infiltrated brain. **a**, **b**, Human neuronal hyperexcitability in glioma. **a**, Top, sagittal brain MRI fluid-attenuated inversion recovery (FLAIR) sequences of adult wild-type IDH cortical glioblastoma in three individuals (human participants 1, 2 and 3, outlined in red, blue and green, respectively). Bottom, intraoperative cortical electrode placement. **b**, Electrocorticography signals (mean high-gamma frequency-filtered power; μV^2) in each of healthy-appearing, tumour core, and tumour-infiltrated brain ($n = 3$ human subjects). Data points expressed as mean value for each subject in each of the three regions, coloured by subject as in **a**. **c**, Mouse neuronal hyperexcitability in paediatric glioma xenograft (SU-DIPG-XIII-FL): plot of presynaptic fibre volley versus amplitude of field EPSP (fEPSP) at varying axonal stimulation intensities (10, 20, 30, 50, 75, 100, 150 and 200 μA) in glioma-bearing or control hippocampus (control: $n = 17$ slices, 3 mice; glioma: $n = 18$ slices, 3 mice at each data point). Data fit to a nonlinear regression and compared using the extra-sum-of-squares F-test; $F = 61.61$, $P < 0.0001$). Representative traces of field responses to varying intensities shown above. Data are mean ± s.e.m. (**b**, **c**). $^*P < 0.05$, one-way analysis of variance (ANOVA) with Tukey's post hoc analysis.

apoptosis in paediatric glioma cells outside of the neuronal microenvironment (Extended Data Fig. 8e, f). By contrast, paediatric glioma cell migration and invasion were influenced by GluA2-DN expression in a cell-intrinsic manner (Extended Data Fig. 8g–j), consistent with previous reports in adult gliomas[25]. Together, these findings indicate that glioma AMPAR activation promotes paediatric glioma growth mainly through microenvironmental interactions such as neuron-to-glioma synaptic transmission.

Next, we sought to therapeutically target glioma currents using existing drugs. Using the AMPAR-blocking anti-epileptic drug perampanel, we found an approximately 50% decrease in paediatric glioma proliferation in perampanel-treated mice compared with vehicle-treated controls (Fig. 4k, Extended Data Fig. 8k). We then targeted gap junction-mediated amplification of neuronal activity-dependent potassium currents using the brain-penetrant gap junction blocker meclofenamate[26]. Meclofenamate treatment similarly decreased paediatric glioma xenograft proliferation and growth (Fig. 4l, Extended Data Fig. 8l).

Gliomas increase neuronal excitability

Neuron–glioma interactions are bidirectional; neuronal activity increases glioma growth[1], and gliomas are thought to increase neuronal activity. In preclinical adult glioblastoma models, gliomas induce neuronal hyperexcitability and seizures[27–29] through non-synaptic glutamate secretion[27,29], secretion of synaptogenic factors[28], and by reducing inhibitory interneurons in the glioma microenvironment[30]. To assess neuronal hyperexcitability in primary human glioblastoma, we performed intraoperative electrocorticography in three awake adult human study participants with cortical high-grade gliomas (IDH wild type) before surgical resection (Fig. 5). High gamma frequency (70–110 Hz) power, a measure that correlates with neuronal firing rate and local field potential[31] and that is increased by cortical hyperexcitability[32], was sampled over a 3-min period while the participants were in a resting state. Outside of the necrotic nodular core of the tumour, we found markedly increased high gamma power in tumour-infiltrated brain compared to healthy-appearing brain (Fig. 5a, b, Extended Data Fig. 9a). Concordantly, we found neuronal hyperexcitability in the microenvironment of paediatric glioma xenografts (Fig. 5c). These findings support the concept[27,28] of hyperexcitable neurons in the glioma microenvironment, which would potentiate mechanisms of activity-regulated glioma progression. As neuronal action potentials result in extracellular rises in potassium[33,34], neuronal hyperexcitability in the glioma microenvironment would promote non-synaptic prolonged glioma potassium currents, as well as synaptic neuron-to-glioma EPSCs (Extended Data Fig. 9b).

Discussion

Membrane depolarization and depolarization-induced calcium transients promote normal development of neural precursor cells, in part through voltage-gated calcium channel signalling[5–9]. Non-synaptic release of neurotransmitters mediates synchronous calcium transients in gap junction-coupled neural precursor cells in many contexts[35–37], but synapses between presynaptic neurons and postsynaptic precursor cells are also well described, including transient synapses onto migrating neuroblasts during corticogenesis[38] and synapses onto OPCs in the developing and adult brain[3,4]. High-grade gliomas integrate into electrical networks and depolarizing current promotes glioma progression similarly to the well-established effect in normal NPCs. In glioma, we have demonstrated bona fide neuron-to-glioma synapses, reminiscent of the synapses found on normal OPCs. In addition, we have shown neuronal activity-evoked potassium currents in glioma cells, reminiscent of activity-dependent currents in normal astrocytes[39]. Neuronal activity-induced glioma membrane depolarization by either mechanism promotes glioma proliferation and growth through voltage-sensitive signalling pathway(s) to be fully elucidated in future work.

Neuronal activity is emerging as a crucial regulator of glioma progression. The electrochemical communication described here joins activity-regulated secretion of growth factors[1,2] as mechanisms that mediate this important microenvironmental interaction. NLGN3, an activity-regulated secreted factor fundamental to glioma progression[2], functions both by stimulating classical oncogenic signalling pathways[1,2] and by promoting neuron-to-glioma synaptogenesis. Appreciating the crosstalk between neurons and the glioma cells invading and integrating into neural circuitry elucidates promising therapeutic targets, including activity-regulated secreted growth factors[1,2], neuron-to-glioma neurotransmission, ion channel function, and gap junction coupling. Modulating the influence of glioma on neuronal excitability represents an important opportunity to dampen the magnitude of activity-regulated glioma growth. Together, the findings presented here identify synaptic neurotransmission and activity-dependent potassium currents as mechanisms that drive glioma growth and illustrate the previously unexplored potential to target glioma circuit dynamics for therapy of these lethal cancers.

Online content

Any methods, additional references, Nature Research reporting summaries, source data, extended data, supplementary information, acknowledgements, peer review information; details of author contributions and competing interests; and statements of data and code availability are available at https://doi.org/10.1038/s41586-019-1563-y.

Received: 28 September 2018; Accepted: 12 August 2019;
Published online 18 September 2019.

1. Venkatesh, H. S. et al. Neuronal activity promotes glioma growth through neuroligin-3 secretion. *Cell* **161**, 803–816 (2015).
2. Venkatesh, H. S. et al. Targeting neuronal activity-regulated neuroligin-3 dependency in high-grade glioma. *Nature* **549**, 533–537 (2017).
3. Bergles, D. E., Roberts, J. D., Somogyi, P. & Jahr, C. E. Glutamatergic synapses on oligodendrocyte precursor cells in the hippocampus. *Nature* **405**, 187–191 (2000).
4. Káradóttir, R., Cavelier, P., Bergersen, L. H. & Attwell, D. NMDA receptors are expressed in oligodendrocytes and activated in ischaemia. *Nature* **438**, 1162–1166 (2005).
5. LoTurco, J. J., Owens, D. F., Heath, M. J., Davis, M. B. & Kriegstein, A. R. GABA and glutamate depolarize cortical progenitor cells and inhibit DNA synthesis. *Neuron* **15**, 1287–1298 (1995).
6. Luk, K. C. & Sadikot, A. F. Glutamate and regulation of proliferation in the developing mammalian telencephalon. *Dev. Neurosci.* **26**, 218–228 (2004).
7. Liu, X., Wang, Q., Haydar, T. F. & Bordey, A. Nonsynaptic GABA signaling in postnatal subventricular zone controls proliferation of GFAP-expressing progenitors. *Nat. Neurosci.* **8**, 1179–1187 (2005).
8. Deisseroth, K. et al. Excitation–neurogenesis coupling in adult neural stem/progenitor cells. *Neuron* **42**, 535–552 (2004).
9. Kougioumtzidou, E. et al. Signalling through AMPA receptors on oligodendrocyte precursors promotes myelination by enhancing oligodendrocyte survival. *eLife* **6**, e28080 (2017).
10. Filbin, M. G. et al. Developmental and oncogenic programs in H3K27M gliomas dissected by single-cell RNA-seq. *Science* **360**, 331–335 (2018).
11. Venteicher, A. S. et al. Decoupling genetics, lineages, and microenvironment in IDH-mutant gliomas by single-cell RNA-seq. *Science* **355**, eaai8478 (2017).
12. Sommer, B., Köhler, M., Sprengel, R. & Seeburg, P. H. RNA editing in brain controls a determinant of ion flow in glutamate-gated channels. *Cell* **67**, 11–19 (1991).
13. Hollmann, M., Hartley, M. & Heinemann, S. Ca^{2+} permeability of KA-AMPA-gated glutamate receptor channels depends on subunit composition. *Science* **252**, 851–853 (1991).
14. Venkataramani, V. Glutamatergic synaptic input to glioma cells drives brain tumour progression. *Nature* https://doi.org/10.1038/s41586-019-1564-x (2019).
15. Oliet, S. H., Malenka, R. C. & Nicoll, R. A. Bidirectional control of quantal size by synaptic activity in the hippocampus. *Science* **271**, 1294–1297 (1996).
16. Bergles, D. E. & Jahr, C. E. Synaptic activation of glutamate transporters in hippocampal astrocytes. *Neuron* **19**, 1297–1308 (1997).
17. Lüscher, C., Malenka, R. C. & Nicoll, R. A. Monitoring glutamate release during LTP with glial transporter currents. *Neuron* **21**, 435–441 (1998).
18. Sibille, J., Pannasch, U. & Rouach, N. Astroglial potassium clearance contributes to short-term plasticity of synaptically evoked currents at the tripartite synapse. *J. Physiol.* **592**, 87–102 (2014).
19. McKhann, G. M. II, D'Ambrosio, R. & Janigro, D. Heterogeneity of astrocyte resting membrane potentials and intercellular coupling revealed by whole-cell and gramicidin-perforated patch recordings from cultured neocortical and hippocampal slice astrocytes. *J. Neurosci.* **17**, 6850–6863 (1997).
20. Osswald, M. et al. Brain tumour cells interconnect to a functional and resistant network. *Nature* **528**, 93–98 (2015).
21. Labrakakis, C., Patt, S., Hartmann, J. & Kettenmann, H. Glutamate receptor activation can trigger electrical activity in human glioma cells. *Eur. J. Neurosci.* **10**, 2153–2162 (1998).
22. Singh, S. K. et al. Identification of human brain tumour initiating cells. *Nature* **432**, 396–401 (2004).
23. Ishiuchi, S. et al. Ca^{2+}-permeable AMPA receptors regulate growth of human glioblastoma via Akt activation. *J. Neurosci.* **27**, 7987–8001 (2007).
24. Sontheimer, H. A role for glutamate in growth and invasion of primary brain tumors. *J. Neurochem.* **105**, 287–295 (2008).
25. Lyons, S. A., Chung, W. J., Weaver, A. K., Ogunrinu, T. & Sontheimer, H. Autocrine glutamate signaling promotes glioma cell invasion. *Cancer Res.* **67**, 9463–9471 (2007).
26. Chen, Q. et al. Carcinoma-astrocyte gap junctions promote brain metastasis by cGAMP transfer. *Nature* **533**, 493–498 (2016).
27. Campbell, S. L., Buckingham, S. C. & Sontheimer, H. Human glioma cells induce hyperexcitability in cortical networks. *Epilepsia* **53**, 1360–1370 (2012).
28. John Lin, C. C. et al. Identification of diverse astrocyte populations and their malignant analogs. *Nat. Neurosci.* **20**, 396–405 (2017).
29. Buckingham, S. C. et al. Glutamate release by primary brain tumors induces epileptic activity. *Nat. Med.* **17**, 1269–1274 (2011).
30. Campbell, S. L. et al. GABAergic disinhibition and impaired KCC2 cotransporter activity underlie tumor-associated epilepsy. *Glia* **63**, 23–36 (2015).
31. Ray, S., Crone, N. E., Niebur, E., Franaszczuk, P. J. & Hsiao, S. S. Neural correlates of high-gamma oscillations (60-200 Hz) in macaque local field potentials and their potential implications in electrocorticography. *J. Neurosci.* **28**, 11526–11536 (2008).
32. Yizhar, O. et al. Neocortical excitation/inhibition balance in information processing and social dysfunction. *Nature* **477**, 171–178 (2011).
33. Hodgkin, A. L. & Katz, B. The effect of sodium ions on the electrical activity of giant axon of the squid. *J. Physiol.* **108**, 37–77 (1949).
34. Ransom, B. R. & Goldring, S. Ionic determinants of membrane potential of cells presumed to be glia in cerebral cortex of cat. *J. Neurophysiol.* **36**, 855–868 (1973).
35. Bittman, K. S. & LoTurco, J. J. Differential regulation of connexin 26 and 43 in murine neocortical precursors. *Cereb. Cortex* **9**, 188–195 (1999).
36. LoTurco, J. J., Blanton, M. G. & Kriegstein, A. R. Initial expression and endogenous activation of NMDA channels in early neocortical development. *J. Neurosci.* **11**, 792–799 (1991).
37. Marins, M. et al. Gap junctions are involved in cell migration in the early postnatal subventricular zone. *Dev. Neurobiol.* **69**, 715–730 (2009).
38. Ohtaka-Maruyama, C. et al. Synaptic transmission from subplate neurons controls radial migration of neocortical neurons. *Science* **360**, 313–317 (2018).
39. Kuffler, S. W. Neuroglial cells: physiological properties and a potassium mediated effect of neuronal activity on the glial membrane potential. *Proc. R. Soc. Lond. B* **168**, 1–21 (1967).

Publisher's note Springer Nature remains neutral with regard to jurisdictional claims in published maps and institutional affiliations.

© The Author(s), under exclusive licence to Springer Nature Limited 2019

METHODS

Mice and housing conditions. All in vivo experiments were conducted in accordance with protocols approved by the Stanford University Institutional Animal Care and Use Committee (IACUC) and performed in accordance with institutional guidelines. Animals were housed according to standard guidelines with free access to food and water in a 12 h light:12 h dark cycle. For brain tumour xenograft experiments, the IACUC does not set a limit on maximal tumour volume but rather on indications of morbidity. In no experiments were these limits exceeded as mice were euthanized if they exhibited signs of neurological morbidity or if they lost 15% or more of their body weight.

Orthotopic xenografting. For all xenograft studies, NSG mice (NOD-SCID-IL2R gamma chain-deficient, The Jackson Laboratory) were used. Male and female mice were used equally. For all immuno-electron microscopy, electrophysiology, single-cell sorting, or calcium imaging experiments, a single-cell suspension from cultured SU-pcGBM2-GFP, SU-DIPG-VI-GFP, SU-DIPG-XIII-FL-GFP, SU-DIPG-VI-GCaMP6s, or SU-DIPG-XIII-FL-GCaMP6s neurospheres were prepared in sterile PBS immediately before the xenograft procedure. Animals at postnatal day (P) 28–30 were anaesthetized with 1–4% isoflurane and placed in a stereotactic apparatus. The cranium was exposed via midline incision under aseptic conditions. Approximately 600,000 cells in 3 μl sterile PBS were stereotactically implanted into the CA1 region of the hippocampus through a 31-gauge burr hole, using a digital pump at infusion rate of 0.4 μl min^{-1} and 31-gauge Hamilton syringe. Stereotactic coordinates used were as follows: 1.5 mm lateral to midline, 1.8 mm posterior to bregma, −1.4 mm deep to cranial surface. At the completion of infusion, the syringe needle was allowed to remain in place for a minimum of 2 min, then manually withdrawn at a rate of 0.875 mm min^{-1} to minimize backflow of the injected cell suspension.

All other xenografts were done using similar techniques with variations in the location of the injection site based on the needs of the experiment. SU-DIPG-XIII-FL-GFP and SU-DIPG-XIII-FL-GluA2-DN-GFP for tumour burden analysis, and SU-DIPG-XIII-FL for meclofenamate treatment, were xenografted into the premotor cortex; stereotactic coordinates used were as follows: 0.5 mm lateral to midline, 1.0 mm anterior to bregma, −1.75 mm deep to cranial surface. SU-DIPG-VI-ChR2, SU-DIPG-XIII-FL-YFP and SU-DIPG-XIII-FL-ChR2 were xenografted more superficially into the premotor cortex to optimize blue light penetration; stereotactic coordinates used were as follows: 0.5 mm lateral to midline, 1.0 mm anterior to bregma, −1.0 mm deep to cranial surface. SU-DIPG-XIII-P*-GFP, SU-DIPG-XIII-P*-GluA2-WT-GFP and SU-DIPG-XIII-P*-GluA2-DN-GFP for survival studies, and SU-DIPG-VI for perampanel treatment were xenografted into the pons; stereotactic coordinates used were as follows: 1.0 mm lateral to midline, −0.8 mm posterior to lambda, −5.0 mm deep to cranial surface.

Fibre optic placement and in vivo optogenetic stimulation. For optogenetic depolarization of glioma, ChR2–YFP (pLV-ef1-ChR2(H134R)-eYFP WPRE) or YFP-only constructs(pLV-ef1-eYFP WPRE) were lentivirally transduced into SU-DIPG-VI and SU-DIPG-XIII-FL cells. YFP-expressing cells were isolated and xenografted into the premotor cortex as described above. Fibre optic placement was performed as previously described[1] after 5 weeks of tumour engraftment. Animals were anaesthetized with 1–4% isoflurane and placed in a stereotactic apparatus. The cranium was exposed using a midline incision under aseptic conditions. A fibre optic ferrule (Doric Lenses) was placed at the premotor cortex (M2) of the right hemisphere using the following coordinates: 0.5 mm lateral to midline, 1.0 mm anterior to bregma, 0.65 mm deep to cranial surface in the right hemisphere. At 6 weeks post-xenograft (allowing a minimum of 7 days of recovery following ferrule placement procedure), all mice were connected to a 100-mW 473-nm DPSS laser system with a mono fibre patch cord, which freely permits wakeful behaviour of the mice. Pulses of light with approximately 5 mW measured output at tip of the patch cord were administered at a frequency of 20 Hz for periods of 30 s, followed by 90 s recovery periods, for a total session duration of 30 min per day for 5 consecutive days. This power represents approximately 30 mW cm^{-2} light density at the tip of the patch cord; with the optical ferrule placed just below the pial surface this would deliver 3 mW cm^{-2} approximately midway through the cortex[40]. Mice were euthanized 24 h after the final (5th) stimulation session.

Bioluminescence imaging. For in vivo monitoring of tumour growth, bioluminescence imaging was performed using an IVIS imaging system (Xenogen). Mice orthotopically xenografted with luciferase-expressing glioma cells were placed under isofluorane anaesthesia and injected with luciferin substrate. Animals were imaged at baseline and randomized based on tumour size by a blinded investigator so that experimental groups contained an equivalent range of tumour sizes. Over the course of each study (described below), all total flux values were then normalized to baseline values to determine fold change of tumour growth.

Mouse drug treatment studies. For all drug studies, NSG mice were xenografted as above with either SU-DIPG-VI or SU-DIPG-XIII-FL cells and randomized to treatment group by a blinded investigator. Four weeks post-xenograft, SU-DIPG-XIII-FL-bearing mice were treated with systemic administration of meclofenamate sodium (20 mg kg^{-1}; Selleck Chemicals; formulated in 10% DMSO in PBS) via intraperitoneal injection for two weeks (5 days per week). Similarly, four weeks post-xenograft, SU-DIPG-VI-bearing mice were treated with oral administration of AMPAR blocker perampanel (0.75 mg kg^{-1}; Adooq Biosciences; formulated in 10% DMSO, 60% PEG300, 30% water) via oral gavage for three weeks (5 days per week). For both studies, controls were treated with an identical volume of the relevant vehicle. Drug treatment began four weeks after xenografting and continued up to week six or seven. Bioluminescence imaging was performed before treatment and every 7 days thereafter using an IVIS imaging system (Xenogen) under isoflurane anaesthesia. Tumour burden was assessed as fold change in total flux from the beginning to end of treatment.

Survival studies. For survival studies, morbidity criteria used were either reduction of weight by 15% initial weight, or severe neurological motor deficits consistent with brainstem dysfunction (that is, hemiplegia or an incessant stereotyped circling behaviour seen with ventral midbrain dysfunction). Kaplan–Meier survival analysis using log rank testing was performed to determine statistical significance.

Single-cell sequencing analysis. We combined publicly available single-cell datasets processed and annotated previously[10,11], all sequenced using smart-seq2 protocol. Following the quality-control measures taken in these studies, we filtered the data to keep cells with more than 400 detected genes, and genes that were expressed in more than 3 cells. We assessed the single-cell transcriptome from 5,096 adult IDH-mutant glioma cells derived from 10 study participants, 599 adult wild-type IDH glioma cells derived from 3 study participants, and 2,259 paediatric H3K27M DMG cells derived from 6 study participants. Malignant cells were inferred by expression programs and detection of tumour-specific genetic alterations. For each sample, we performed first cell-level normalization, and then centred the gene expression around 0 to allow principal component analysis (PCA) computation. Following the PCA reduction, we clustered the cells using shared nearest neighbour clustering. We examined the synapse signature of each of the cells in each cluster by taking the mean expression of genes listed below, and subtracting the average expression of a control set of genes chosen from the same expression distribution (as previously described[11]).

Xenograft dissociation for single-cell analysis. NSG mice were euthanized six weeks after patient-derived DIPG cell lines (SU-DIPG-VI and SU-DIPG-XIII-FL were xenografted into the right hippocampus as described above. The brain was isolated and sliced on a Leica vibratome VT1200S at a thickness of 350 μm. Acute brain slices were placed in oxygenated artificial cerebrospinal fluid before being visually inspected under a fluorescent microscope for presence and proper placement of GFP^+ DIPG cells. Slices containing DIPG cells were then minced with a scalpel and enzymatically dissociated using the Miltenyi brain tumour dissociation kit P (130-095-942). The resultant cell suspension was passed through a 70-μm SmartStrainer from Miltenyi (130-098-462). Myelin debris was then removed using the Miltenyi myelin removal beads II (130-096-733).

Fluorescence-activated cell sorting. Cell suspensions from xenograft dissociation were stained with APC/Cy7 anti-human HLA-A, B, C from Biolegend (311426) and Calcein Violet 450 AM Viability Dye from eBioscience (65-0854-39). Gates were first drawn to exclude calcein negative (dead) cells. Double-positive, viable DIPG cells (HLA^+ and GFP^+) were index sorted on a FACSAria Fusion Special Order Instrument (Becton Dickinson) as singlets by adhering to a strict forward scatter by area gating scheme. Cells were sorted into skirted 96-well plates, each well of which contained 4 μl of lysis buffer as previously described[41].

Whole-transcriptome amplification, library construction, sequencing and processing. Single sorted cells in 96-well plates were processed using the smart-seq2 protocol as previously described[41]. Next-generation sequencing libraries were then generated using the Nextera XT kit from Illumina (FC-131-1096) and cells were multiplexed in batches of 96 using the IDT for Illumina dual-unique indexing scheme (20027213). All pools were sequenced in paired-end mode on the Illumina Next500 to an average target depth of approximately 1 million reads per cell with mid-output kits (130 million reads). Paired-end, 75-base-pair reads were mapped to the UCSC hg19 human transcriptome using Bowtie 0.12.7 with parameters -q–phred33-quals -n 1 -e 99999999 -l 25 -I 1 -X 2000 -a -m 15 -S -p 6', which allows alignment of sequences with single base changes, such as point mutations in the *H3F3A* (also known as *H3-3A*) gene. Expression values were calculated from SAM files using RSEM 1.2.19 in paired-end mode using parameters '–estimate-rspd–paired end -sam -p 6', from which transcript per million (TPM) values for each gene were extracted. Matrices of TPM values were then processed and analysed using the Seurat (v.2.0) package. Individual cells were scored for their expression of a curated housekeeping gene set and then TPM values were normalized, analysed for variable gene expression and scaled for downstream dimensionality reduction. PCA was run and then clusters defined from significant PCs.

2D plots. 2D plots were generated by methods previously described[42]. For the DIPG biopsies and xenografts plots, the *y*-axis value for each cell was calculated as the difference between an OPC-like stem-cell signature specific to the H3K27M-mutant glioma cells and the sum of astroglial and oligodendroglial-differentiation scores previously defined[10]. In other words, increasing *y*-values correspond to

stronger stem-like characteristics. Conversely, negative *y*-values indicate a differentiated cell state. The *x* axis was plotted by assessing each cell for astroglial and oligodendroglial module scores and plotting the larger value of the two. If a cell scored negatively for both differentiation scores, it was assigned a value of zero and jitter was applied to the ggplot function in R to facilitate visualization of these cells (height = 0.1, width = 0.1). Lastly, if a cell scored more highly for the astroglial than oligodendroglial module, then the sign of the astroglial score was switched to allow for plotting both differentiation paths along one axis. Plots were generated using ggplot in RStudio 1.0.136.

Derivation of synapse gene set from DMG/DIPG biopsies. In the case of DMG biopsies, the OPC score is the OPC-shared score previously defined[10]. The DIPG synapse score was derived from a single biopsy (BCH869) by a method described below and is distinct from the OPC-shared score. After removal of non-malignant cells, DIPG biopsy BCH869 was isolated for analysis via the Seurat (v.2.0) pipeline. TPM expression values were normalized and variable genes were identified. Data were then scaled for dimensionality reduction via PCA and *t*-distributed stochastic neighbour embedding (*t*-SNE). Shared nearest neighbour clustering of DIPG cells revealed a cluster statistically enriched for genes involved in synapse formation and function. The resulting synaptic gene set used is as follows: *PTPRS*, *ARHGEF2*, *GRIK2*, *DNM3*, *LRRTM2*, *GRIK5*, *NLGN4X*, *NRCAM*, *MAP2*, *INA* and *TMPRSS9*.

Signature correlations. To compute a gene signature for a set of genes, we use the function AddModuleScore by Seurat[43] package, which calculates the average expression levels of the gene set subtracted by the aggregated expression of 100 randomly chosen control gene sets, where the control gene sets are chosen from matching 25 expression bins corresponding to the tested gene set expression. To calculate the correlation between two gene expression scores we used Pearson correlation and report the correlation coefficient (rho) and the Pearson *P* value.

Patient-derived cell culture and primary tissue samples. For all human tissue studies, informed consent was obtained and tissue was used in accordance with protocols approved by the Stanford University Institutional Review Board (IRB). For all patient-derived cultures, mycoplasma testing was routinely performed and short tandem repeat DNA fingerprinting was performed every three months to verify authenticity.

All high-grade glioma cultures were generated as previously described[1]. In brief, tissue was obtained from high-grade glioma (WHO (World Health Organization) grade III or IV) tumours at the time of biopsy or from early post-mortem donations. Tissue was dissociated both mechanically and enzymatically and grown in a defined, serum-free medium designated 'tumour stem media' (TSM), consisting of neurobasal(-A) (Invitrogen), B27(-A) (Invitrogen), human bFGF (20 ng ml^{-1}; Shenandoah), human EGF (20 ng ml^{-1}; Shenandoah), human PDGF-AA (10 ng ml^{-1}) and PDGF-BB (10 ng ml^{-1}; Shenandoah) and heparin (2 ng ml^{-1}; Stem Cell Technologies).

The short tandem repeat fingerprints and clinical characteristics for the patient-derived cultures and xenograft models used have been previously reported[1,2,44,45] with the exception of SU-DIPG25 which is X/X (AMEL), 12/12 (CSF1PO1), 8/11 (D13S317), 12/13 (D16S539), 30/35 (D21S11), 11/13 (D5S818), 10/12 (D7S820), 9/9 (TH01), 7/8 (TPOX), 14/18 (vWA). SU-DIPG25 is a H3.3K27M mutant tumour that was derived from the brainstem at the time of autopsy from a female who was 5 years of age, treated with radiotherapy, and survived 11 months (clinical characteristics are also reported in Extended Data Table 1).

Primary tissue sample SU-DIPG39 is a H3.3K27M mutant tumour that was derived from the brainstem at the time of autopsy from a male who was 5 years of age at diagnosis, treated with radiotherapy, and survived 6 months. Primary tissue sample SU-GBM092 is an adult hemispheric high-grade glioma, sampled at the time of autopsy from a male who was 47 years of age at diagnosis, treated with surgical resection, radiotherapy and temozolomide, and survived 6 months. Clinical characteristics of all primary tissue samples are described in Extended Data Table 1.

PSD95-RFP cloning. PSD95-pTagRFP (plasmid 52671) was purchased from Addgene. Primers were used to excise and amplify the PSD95-pTagRFP ORF from the original vector. This amplicon was inserted by Gibson cloning (New England Biolabs E2611) downstream of an EF1α-promoter in a pCDH vector (System Biosciences CD811A-1) linearized by XbaI and NotI. Forward primer for Gibson assembly: 5′-AAATCGGATCCGCGGCCGCGGCCACCATGGACTGTCTC-3′ and reverse primer for Gibson assembly: 5′-ATCCAGAGGTTGATTGTCGAT CAATTAAGTTTGTGCCCCAG-3′. A *PGK1* promoter in the same plasmid drives GFP expression. Once cloned, the plasmid was packaged together with helper plasmids (pΔ8.9 and VSV-g) to generate replication-deficient lentivirus from adherent 293T cells. One million target SU-DIPG-VI or SU-DIPG-XIII-FL cells were infected with Lenti-X (Takara) concentrated viral supernatant and allowed to recover for 1 week. RFP-positive cells were isolated for purity by FACS (BD FACS Aria) and returned to culture.

Neuron–glioma co-culture experiments. Neurons were isolated from the brains of P_1 NSG;wild-type *Nlgn3* or NSG;*Nlgn3^{KO}* mice (The Jackson Laboratory) using the Neural Tissue Dissociation Kit - Postnatal Neurons (Miltenyi), and followed by the Neuron Isolation Kit, Mouse (Miltenyi) per manufacturer's instructions. After isolation, 300,000 neurons were plated onto circular glass coverslips (Electron Microscopy Services) pre-treated for 1 h at room temperature with poly-l -lysine (Sigma) and then 3 h at 37 °C with 5 μg ml^{-1} mouse laminin (Thermo Fisher). Neurons are cultured in BrainPhys neuronal medium (StemCell Technologies) supplemented with 1× glutamax (Invitrogen), penicillin/streptomycin (Invitrogen), B27 supplement (Invitrogen), BDNF (10 ng ml^{-1}; Shenandoah), and GDNF (5 ng ml^{-1}; Shenandoah), TRO19622 (5 μM; Tocris), β-mercaptoethanol (Gibco), and 2% fetal bovine serum. Half of the medium was replenished on days in vitro (DIV) 1 and UFDU was added at 1 μM. This was repeated at DIV 3. On DIV 5, half of the medium was replaced with serum-free in the morning. In the afternoon, the medium was again replaced with half serum-free medium containing 75,000 glioma cells expressing PSD95–RFP. Glioma cells were cultured with neurons for 72 h and then fixed with 4% paraformaldehyde (PFA) for 20 min at room temperature and stained for immunofluorescence analysis as described below.

Synaptic puncta staining and visualization. For immunohistochemistry, fixed coverslips were incubated in blocking solution (3% normal donkey serum, 0.3% Triton X-100 in TBS) at room temperature for 1 h. Primary antibodies mouse anti-nestin (1:500, Abcam), guinea pig anti-synapsin1/2 (1:500; Synaptic Systems), rabbit anti-RFP (1:500; Rockland), or chicken anti-neurofilament (M+H; 1:1,000; Aves Labs) were diluted in antibody diluent solution (1% normal donkey serum in 0.3% Triton X-100 in TBS) and incubated overnight at 4 °C. Samples were then rinsed three times in TBS and incubated in secondary antibody solution (Alexa 488 donkey anti-chicken IgG; Alexa 594 donkey anti-rabbit IgG, Alexa 647 donkey anti-mouse IgG, and Alexa 405 donkey anti-guinea pig IgG all used at 1:500 (Jackson Immuno Research)) in antibody diluent solution at 4 °C overnight. Coverslips were rinsed three times in TBS and mounted with ProLong Gold Mounting medium (Life Technologies). Images were collected using a 63× oil-immersion objective on a Zeiss LSM800 confocal microscope and processed with Airyscan. Coverslips were used to quantify colocalization as described below.

Confocal puncta quantification. Colocalization of all synaptic puncta images from neuron–glioma co-cultures described above were analysed using a custom ImageJ processing script written at the Stanford Shriram Cell Science Imaging Facility to define each pre- and postsynaptic puncta and determine colocalization within a defined proximity of 1.5 μM. To partially subtract local background, we used the ImageJ rolling ball background subtraction (https://imagej.net/Rolling_Ball_Background_Subtraction). The peaks were found using the imglib2 DogDetection plugin (https://github.com/imglib/imglib2algorithm/blob/master/src/main/java/net/imglib2/ algorithm/dog/DogDetection.java). In this plugin, the difference of Gaussians is used to enhance the signal of interest using two different sigma: a 'smaller' sigma, which defines the smallest object to be found and a 'larger' sigma, for the largest object. The plugin then identifies the objects that are above the min peak value, and assigns regions of interest (ROIs) to each channel. The number of neuron and glioma ROIs are counted and the script extracts the number of glioma ROIs within 1.5μm of the neuron ROIs. This script was implemented in Fiji/ImageJ[46–48] using the ImgLib2[49] and ImageJ Ops (https://imagej.net/ImageJ_Ops) libraries.

Sample preparation and image acquisition for electron microscopy. Eight to twelve weeks after xenografting, mice were euthanized by transcardial perfusion with Karnovsky's fixative: 2% glutaraldehyde (EMS 16000) and 4% paraformaldehyde (EMS 15700) in 0.1M sodium cacodylate (EMS 12300), pH 7.4. Primary adult glioma tissue taken at surgical resection was fixed in the same solution. Transmission electron microscopy was performed in the tumour mass within the CA1 region of the hippocampus for all xenograft analysis. The samples were then post-fixed in 1% osmium tetroxide (EMS 19100) for 1 h at room temperature, washed 3 times with ultrafiltered water, then en bloc stained for 2 h at room temperature. Samples were dehydrated in graded ethanol (50%, 75% and 95%) for 15 min each at 4 °C; the samples were then allowed to equilibrate to room temperature and were rinsed in 100% ethanol twice, followed by acetonitrile for 15 min. Samples were infiltrated with EMbed-812 resin (EMS 14120) mixed 1:1 with acetonitrile for 2 h followed by 2:1 EMbed-812:acetonitrile for 2 h. The samples were then placed into EMbed-812 for 2 h, then placed into TAAB capsules filled with fresh resin, which were then placed into a 65 °C oven overnight. Sections were taken between 40 and 60 nm on a Leica Ultracut S (Leica) and mounted on 100-mesh Ni grids (EMS FCF100-Ni). For immunohistochemistry, microetching was done with 10% periodic acid and eluting of osmium with 10% sodium metaperiodate for 15 min at room temperature on parafilm. Grids were rinsed with water three times, followed by 0.5 M glycine quench, and then incubated in blocking solution (0.5% BSA, 0.5% ovalbumin in PBST) at room temperature for 20 min. Primary rabbit anti-GFP (1:300; MBL International) was diluted in the same blocking solution and incubated overnight at 4 °C. The next day, grids were rinsed in PBS three times, and incubated in secondary antibody (1:10 10-nm gold-conjugated IgG TED Pella 15732) for one hour at room temperature and rinsed with PBST followed by water. For each staining set, samples that did not contain any GFP-expressing cells were stained simultaneously to control for any non-specific binding. Grids were contrast stained for 30 s in 3.5% uranyl acetate in 50% acetone followed by staining in 0.2%

lead citrate for 90 s. Samples were imaged using a JEOL JEM-1400 TEM at 120 kV and images were collected using a Gatan Orius digital camera.

Electron microscopy data analysis. Sections from the xenografted hippocampi of mice were imaged as above using TEM imaging. Here, 101 sections of SU-DIPG-VI across 3 mice and 104 sections of SU-DIPG-XIII-FL across 3 mice were analysed. Electron microscopy images were taken at 6,000× with a field of view of 15.75 μm^2. Synapses were inspected by two distinct investigators, including board-certified neuropathologist H.Vogel. Glioma cells were counted and analysed after unequivocal identification of immunogold particle labelling with three or more particles. Furthermore, to determine synaptic structures all three of the following criteria had to be clearly met: (1) presence of synaptic vesicle clusters; (2) visually apparent synaptic cleft; and (3) identification of clear postsynaptic density in the glioma cell. To quantify the percentage of glioma cells that form synaptic structures, the number of glioma–neuron synapses identified was divided by the total number of glioma cells analysed.

Slice preparation for electrophysiology and calcium imaging experiments. Hippocampal slices (225-μm thick) were prepared from mice (4–8 weeks after xenografting) in accordance with a protocol approved by Stanford University APLAC as previously described[50] and maintained for 30 min in warm (30 °C) oxygenated (95% O_2, 5% CO_2) artificial cerebrospinal fluid (ACSF) containing (in mM): 119 NaCl, 26 $NaHCO_3$, 10 glucose, 2.5 KCl, 1 NaH_2PO_4, 1.3 $MgSO_4$ and 2.5 $CaCl_2$ before being allowed to equilibrate at room temperature for an additional hour.

Electrophysiology. Slices were transferred to a recording chamber and perfused with oxygenated, warmed (28–30 °C) ACSF containing picrotoxin (50 μM). In some experiments, $CaCl_2$ was replaced with $SrCl_2$ (4 mM). GFP-labelled glioma cells were identified with an epifluorescent microscope equipped with DIC optics (Olympus BX50WI). Whole-cell recording pipettes (3–5 MΩ) were filled with a solution containing (in mM): 135 $CsMeSO_4$, 12 HEPES, 8 NaCl, 0.25 EGTA, 2 $MgCl_2$, 1 Mg_2ATP, 0.3 Na_3GTP and 5 phosphocreatine for voltage-clamp recordings ($CsMeSO_4$ was replaced with equimolar $KMeSO_4$ for current-clamp recordings; pH adjusted to 7.4, 292–296 mOsM). In some experiments biocytin (0.5%) was added to the pipette solution. Glioma and CA1 pyramidal cells were voltage-clamped at −80 mV and −70 mV, respectively. Synaptic responses were evoked with a bipolar electrode placed near the DIPG cells in strata radiatum or, in some cases, strata oriens to maximize the chance of activating a synaptic input onto the cells. Population fEPSPs were recorded with a pipette filled with 1 M NaCl solution containing 10 mM HEPES (pH adjusted to 7.4) and placed in proximal strata radiatum of CA1. fEPSPs for input–output experiments (Fig. 5c) were recorded in picrotoxin-free ACSF. Field recordings from xenografted slices were interleaved with control slices from the non-xenografted contralateral hippocampus of the same mouse. The sensitivity of glioma cells to extracellular K^+ was performed in the presence of d-2-amino-5-phosphonovalerate (d-AP5; 100 μM), NBQX (10 μM) and TTX (0.5 μM) to block neuronal activity. Optogenetic currents were evoked with a 470-nm collimated LED connected to the microscope and controlled by a t-cube LED driver (Thorlabs). Stimulation duration, frequency and intensity were set by a Master 8 programmable pulse generator (A.M.P.I.) connected to an Iso-flex stimulus isolator (A.M.P.I.) for synaptic stimulation, to the LED driver for optogenetic stimulation, or to a Picospritzer II (Parker Hannifin Corp.) for local application of (*S*)-AMPA (6 psi, 1 s). Synaptic, optogenetic and agonist-induced signals were acquired with a MultiClamp 700B amplifier (Molecular Devices) and digitized at 10 kHz with a National Instruments data acquisition device (BNC-2090). Data were recorded and analysed using a custom program written for Igor Pro software (Wavemetrics). For representative traces shown in Figs. 2c– h, 3a, b, e, 5c, Extended Data Figs. 3d, 5a, d, e, h, 6c and i, stimulus artefacts preceding the EPSC, EPSP or field potential have been removed for clarity.

Inhibitors. Drugs and toxins used for electrophysiology were picrotoxin (50 μM; Sigma), TTX (0.5 μM; Tocris), NBQX (10 μM; Tocris), NASPM (100 μM; Tocris), d-AP5 (100μM; Tocris), carbenoxolone (100 μM; Alfa Aesar), meclofenamate (100 μM; Selleckchem), (*S*)-AMPA (500 μM; Tocris), cyclothiazide (100 μM; Tocris), TBOA (200 μM; Tocris), and biocytin (Invitrogen). When used for in vitro slice application, drugs were made up as a 1,000× stock in distilled water or dimethylsulfoxide (DMSO) and dissolved to their final concentrations in ACSF before exposure to slices.

Calcium imaging. For calcium imaging, the genetically encoded calcium indicator GCaMP6s was lentivirally transduced into SU-DIPG-VI and SU-DIPG-XIII-FL (pLV-ef1-GCaMP6s-P2A-nls-tdTomato). In this case, glioma cells containing the GCaMP6s reporter can be identified using the tdTomato nuclear tag. These cells were isolated and xenografted into the CA1 region of the hippocampus as described above. Xenografts were post-fixed and stained for tdTomato and human nuclei markers to ensure only glioma cells expressed the construct (Extended Data Fig. 4).

Two-photon calcium imaging experiments were performed using Prairie Ultima XY upright two-photon microscope for tissue slices equipped with an Olympus LUM Plan FI W/IR-2 40× water immersion objective. The temperature of the perfusion media, ACSF as described above, was kept at 30 °C, and perfused through the system at rate of 2 ml min^{-1}. Excitation light was provided at a wavelength of 920 nm through a tunable Ti:Sapphire laser (Spectra Physics Mai Tai DeepSee) to allow for excitation of both tdTomato and GCaMP6s. The actual laser power reaching the scanhead for each scope is dynamically controlled by Pockels cells via software interface. Pockels cell were set at 10 for all experiments, and PMTs were set at 800 for each channel. For these settings, power at back aperture of the objective was approximately 30 mW at 920 nm. The wavelength ranges for the emission filters were PMT1: 607 nm centre wavelength with 45 nm bandpass (full-width at half-maximum) and PMT2: 525-nm centre wavelength with 70-nm bandpass (full-width at half-maximum). Recordings were made at 0.65 frames per second (~1.5 Hz) for about 30 min in the case of spontaneous activity and 10 min in the case of response to periodic electrical stimulation. Cells were identified via the expression for the nuclear tdTomato tag and were only imaged in the area of interest, specifically in the CA1 region of the hippocampus. Similar to the electrophysiology paradigm, for neuronal stimulation experiments, the electrode was placed in the hippocampus to stimulate the neuronal inputs originating in CA3. For electrical stimulation, approximately 20 μA over 200 μs was delivered to local axons using a stimulating bipolar microelectrode. For all inhibitor experiments, inhibitors were directly diluted into the ACSF perfusion media at desired concentration, oxygenated, and delivered to the slices through the perfusion system.

Calcium imaging analysis. Two-photon live image sequences were analysed using a custom image processing pipeline at the Stanford Shriram Cell Science Imaging Facility. To correct for any motion artefact we identify the relative shift between adjacent images in the 'nucleus' (tdTomato) channel using cross-correlation[51] and applied the correction to both the nucleus and calcium channels. To segment the image into regions representing individual cells we first divide the image into superpixels using the simple linear iterative clustering (SLIC)[52]. We then manually adjust a threshold to separate background superpixels from foreground (cells) superpixels using their median intensity. The $\Delta F/F$ traces of each cell were computed by subtracting the mean intensity of the cell at every time point with the twentieth percentile of an adjustable time window preceding the time point and dividing it by the same number. To find the local maxima of calcium signals, the data are first smoothed using a 20-frame window and peaks are found using an algorithm written by Marco Duarte (http://nbviewer.jupyter.org/github/demotu/BMC/blob/master/notebooks/DetectPeaks.ipynb). To measure synchronicity between cells, we used the definition previously proposed[20]. Synchronous cells, the number of synchronous communications, and the time point of the synchronous firing were determined using a window of six frames (about 4 s) around each peak. The correlation image for each pixel is computed by averaging the correlation coefficients (taken over time) of each pixel with its four immediate neighbours[53]. This algorithm was implemented in Python using the scikit-image library[54]. Full 30-min spontaneous activity was assessed for synchronicity in Fig. 3h, however for clarity, only 10 min of analysis is shown in Extended Data Fig. 5i. For gap junction blocker, CBX experiments, synchronicity was calculated for spontaneous transients over the course of 15 min in multiple xenografts. CBX was then perfused through the media, and calcium transients were recorded for another 15 min. Transients were analysed for synchronicity as above before and after addition of inhibitor.

Quantitative fluorescence intensity analysis was done on calcium transients that were reliably evoked by axonal stimulation. To determine the effect of tetrodotoxin on the calcium transients in response to electrical stimulation of the CA3 Schaffer collaterals, the field of cells were stimulated three times in 1-min intervals to ensure synaptic connectivity. TTX (500 μM) was then perfused into the slices and the stim repeated on the same field of cells to gauge direct effect of TTX on stimulation response. For analysis, ROIs of each responding nucleus were set and $\Delta F_{max}/F_0$ (maximum difference in fluorescence intensity normalized to background fluorescence) measurements were determined as above before and after TTX treatment.

Perfusion and immunohistochemistry. Animals were anaesthetized with intraperitoneal avertin (tribromoethanol), then transcardially perfused with 20 ml of PBS. Brains were fixed in 4% PFA overnight at 4 °C, then transferred to 30% sucrose for cryoprotection. Brains were then embedded in Tissue-Tek O.C.T. (Sakura) and sectioned in the coronal plane at 40 μm using a sliding microtome (Microm HM450; Thermo Scientific).

For immunohistochemistry, coronal sections were incubated in blocking solution (3% normal donkey serum, 0.3% Triton X-100 in TBS) at room temperature for 30 min. Chicken anti-GFP (1:500, Abcam), mouse anti-human nuclei clone 235-1(1:100; Millipore), rabbit anti-Ki67 (1:500; Abcam), rabbit anti-cleaved caspase 3 (1:200, Cell Signaling), mouse anti-MAP2 (1:1,000; Millipore), mouse anti-vimentin, (1:500; Dako), rabbit anti-histone H3.3K27M mutant (1:500; Millipore), mouse anti-nestin (1:500, Abcam), or Streptavidin Alexa Fluor 594 conjugate (1:500, Thermo Fisher), were diluted in antibody diluent solution (1% normal donkey serum in 0.3% Triton X-100 in TBS) and incubated overnight at 4 °C. Sections were then rinsed three times in TBS and incubated in secondary antibody solution (Alexa 488 donkey anti-chicken IgG; Alexa 594 donkey anti-rabbit IgG, Alexa 647 donkey anti-mouse IgG, Alexa 405 donkey anti-guinea pig IgG, Alexa 647 donkey anti-rabbit IgG, or Alexa 594 donkey anti-mouse IgG all used at 1:500 (Jackson Immuno Research) in antibody diluent at 4 °C overnight. Sections were

rinsed three times in TBS and mounted with ProLong Gold Mounting medium (Life Technologies).

Confocal imaging and quantification of cell proliferation and tumour burden. Cell quantification within xenografts was performed by a blinded investigator using live counting on a 40× oil immersion objective of a Zeiss LSM700 scanning confocal microscope and Zen 2011 imaging software (Carl Zeiss). For Ki67 analysis, the area for quantification was selected as follows: for a 1-in-6 series of 40-μm coronal sections, 4 consecutive sections were selected. For optogenetic studies, because approximately 10% of the light reaches 0.5 mm through the cortex (roughly midway)[40], in each of the four consecutive sections, four 160 × 160-μm field areas for quantification were selected in superficial cortical layer 2/3 through layer 5A/B of M2.

For overall tumour burden analysis of SU-DIPG-XIII-FL-GluA2-DN-GFP mice (Fig. 4i, j), the area for quantification was selected as follows: for a 1-in-2 series of 40-μm coronal sections, 6 consecutive sections were selected at approximately 1.1–0.86 mm anterior to bregma; using our stereotactic coordinates for tumour xenograft, these sections are expected to include the tissue most proximal to the site of tumour cell implantation in the coronal plane. Whole tissue slices were imaged simultaneously and imaged for total human nuclei and glioma derived GFP. Confocal microscopy images were analysed using a custom image processing script written at the Stanford Shriram Cell Science Imaging Facility. To isolate the brain section, we use the ImageJ IJ_IsoData threshold algorithm. First, we did a partial local background subtraction using the ImageJ rolling ball background subtraction followed by a Gaussian blur using a sigma of 7. Then, to isolate the foreground pixels, we used the ImageJ Triangle threshold algorithm. Data are presented as mean intensity (total intensity/area of slice).

For overall GFP^+ cell outgrowth analysis of SU-DIPG-XIII-P*-GluA2-DN-GFP xenografts (Fig. 4g), both overall human nuclei and GFP were imaged for analysis. The percentage GFP was noted based on the ratio of the overall GFP/HNA signal as a measure of the percentage of glioma cells co-labelled with GFP.

For drug treatment studies, a 1-in-6 series of coronal brain sections were selected with 4 consecutive slices (4 fields per slice) analysed with respect to overall tumour burden. Within each field, all HNA-positive and GFP-positive tumour cells were quantified to determine tumour burden within the areas quantified. HNA-positive and GFP-positive tumour cells were then assessed for co-labelling with Ki67. To calculate the proliferation index (the percentage of proliferating tumour cells for each mouse), the total number of HNA-positive and GFP-positive cells co-labelled with Ki67 across all areas quantified was divided by the total number of cells counted across all areas quantified ($Ki67^+/GFP^+/HNA^+$).

To measure cell apoptosis, cleaved caspase-3 was co-localized with HNA in stimulated and mock-stimulated brain tissue. Tissue was stained in a 1-in-12 series, and three tumour-containing slices were selected for analysis. Tiled confocal images were taken of the entire tumour region in each slice using a 20× objective, and total counts of caspase-3^+/HNA^+ cells were assessed.

GluA2 editing efficiency. RNA was extracted using TRIZOL based on the manufacturer's instructions from three sets of cell pellets obtained from the same flask. Then, 600 ng of RNA was incubated with 1 μl of DNaseI (Maxima First Strand cDNA Synthesis Kit for RT-qPCR) and 1 μl of DNaseI buffer brought to a total volume of 10 μl at 37 °C for 2 min and cooled down in ice for 2 min. Four microliters of 5X Reaction mix and 1 μl of Maxima Enzyme mix were added to the DNase-I-treated reaction and brought to a total volume of 20 μl with the addition of nuclease-free water. The tubes were incubated at 25 °C for 10 min, followed by 65 °C for 15 min, and the reaction was terminated by heating at 85 °C for 5 min. For each reaction, we also ran a reverse transcriptase minus control sample.

The GluA2 PCR nested primers were as previously described[55]. The first PCR was done using accuprime Taq HiFi (ThermoFisher Scientific) on 2 μl cDNA and 10 μM primers (GluA2-F1: 5′-TTCCTGGTCAGCAGATTTAGCC-3′; GluA2-R1: 5′-TTCCCTTTGGACTTCCGCAC-3′) in 50 μl total volume. Initial denaturation was done for 2 min at 94 °C; followed by 37 cycles of denaturation for 30 s at 94 °C, annealing for 30 s at 60 °C, and extension for 30 s at 68 °C. Final extension was done for 2 min at 68 °C. The nested PCR was done using 2 μl of the first PCR product and primers (GluA2-F1 and GluA2-R2: 5′-TGGGAGACACCATCCTCTCTACAG-3′) at similar PCR conditions, except annealing was done at 65 °C. The correct size bands were cut and gel extraction was done using a Qiagen kit (28706). Then, 800 ng of eluted DNA was digested with 2 U of BbvI enzyme and 10× Cutsmart buffer in a total volume of 40 μl at 37 °C for 12 h and the reaction was stopped at 65 °C for 2 min. The digested volume was cleaned up using Zymo DNA cleanup kit and submitted to Agilent Bioanalyzer QC. The editing efficiency of GluA2 was calculated by dividing the molarity of 228-bp band (edited) with the molarity of 49-bp band (both edited and unedited).

Quantitative PCR. Primers were synthesized from Elim Biopharm based on those previously described[55]. RNA was extracted using TRIZOL based on manufacturer's instructions from 500,000 cells in a 6-well plate with 1 ml growth media 24 h after passaging. cDNA synthesis was performed exactly as above. Both no-template control and reverse transcriptase minus control were included. qPCR was performed in a BIO-RAD thermocycler in triplicate. cDNA was diluted 1:10 with water, and 2 μl was used in the PCR reaction along with 5 μl of Maxima SYBR Green/ROX qPCR Master Mix (2X) (Thermo Fisher Scientific, K0222) and 3 μM qPCR primers, all brought to a total volume of 10 μl. β-actin (*ACTB*) was used as an endogenous control and data were normalized based on the ΔC_t method. Oligonucleotides used were as follows: *ADAR1* qPCR-F1, 5′-GATGCCTTTGCAGAACACCA-3′; *ADAR1* qPCR-R1, 5′-TGCCTTCTGATGCTGAGAACC-3′; *ACTB* qPCR-F, 5′-CGAGGACTTTGATTGCACAT-3′; *ACTB* qPCR-R, 5′-ACACGAAAGCAATGCTATCA-3′.

Dominant-negative GluA2 cloning. To generate dominant-negative GluA2 subunits of the AMPAR, we carried out two amino acid substitutions in the pore region: methionine to arginine (M/R: 606), and glutamine to arginine (Q/R: 607); AMPARs that incorporate this subunit are non-conducting[56]. We obtained the CAG-EGFP-GluA2-DN construct generated by A. Agarwal and D. Bergles and cloned the eGFP-GluA2-DN region from the original CAG-eGFP-GluA2-DN (pAA018) into a lentiviral system. We introduced Mlu-I with Kozak sequence (5′-TAAGCAACGCGTGCCACCATGGTGAGCAAGGGCGAG-3′) and Xma-I restriction sites (5′-TGCTTACCCGGGCTAAATTTTAACACTCTC-3′) on the 5′ eGFP end and 3′ GluA2-DN, respectively by PCR. Then 1 μg of pLV-EF1a-IRES-Hygro (Addgene 85134) was digested with MluI-HF and XmaI in NEB cutsmart buffer overnight at 37 °C to remove the IRES-HYGRO region. The digested product was run on a 1% agarose gel and the correct digested band was gel purified using Qiagen gel extraction kit. At a 20 ng μl^{-1} concentration, the digested vector was treated with FAST Alkaline Phosphatase (FERMENTAS) at 37 °C for 10 min and deactivated at 75 °C for 5 min. Then, 300 ng of the PCR product with restriction sites was digested with MluI-HF and XmaI for 30 min and column purified using Zymo DNA Clean & Concentrator-5 D4013. The vector and insert were ligated at 5:1 insert DNA: vector DNA using T4 DNA ligase (EL0011; Fisher Scientific) for 1 h at room temperature. The cells were transformed in homemade Stbl3 cells overnight and the colonies were picked the next day and sent for Sanger sequencing to ElimBio.

Wild-type GluA2 cloning. We introduced SpeI (5′-TAAGCAACTAGTATGCAAAAGATTATGCAT-3′) and XmaI (5′-TGCTTACCCGGGCTAAATTTTAACACTTTCGAT-3′) restriction sites in full-length human GRIA2 clone (GluA2 WT) obtained from Origene (RC212599) by PCR. Then, 1 μg of pLV-EF1a-eGFP-GluA2DN was digested with SpeI-HF and XmaI in NEB cutsmart buffer overnight at 37 °C to remove the GluA2-DN region. The digested product was run on a 1% agarose gel and the correct digested band was gel-purified using Qiagen gel extraction kit. At a 20 ng μl^{-1} concentration, the digested vector was treated with FAST Alkaline Phosphatase (FERMENTAS) at 37 °C for 10 min and deactivated at 75 °C for 5 min. Then, 300 ng of the PCR product with restriction sites was digested with SpeI-HF and XmaI for 30 min and column-purified using Zymo DNA Clean & Concentrator-5 D4013.The vector and insert were ligated and cells were transformed as described above.

CellTiter-Glo assay. To assess overall cell number, 5,000 SU-DIPG-XIII-FL-GFP or SU-DIPG-XIII-FL-GluA2-DN-GFP glioma cells were seeded in growth media in a 96-well plate. After 24, 48 or 72 h, CellTiter-Glo reagent (Promega) was added at a 1:1 ratio. Luminescence was measured after a 10-min incubation at room temperature to stabilize the signal.

3D invasion and migration assays. 3D invasion assays were performed as previously described[57] with some modifications. In brief, in ULA 96-well round-bottomed plates (Costar, Corning Inc.), 50 μl of Matrigel Basement Membrane Matrix (Corning Life Sciences) was added to each well containing neurospheres of approximately 200 μm in diameter in 50 μl of media. The plates were incubated at 37 °C, 5% CO_2, 95% humidity for 1 h before addition of 50 μl per well of culture medium. Images were obtained using the Cytation 5 Cell Imaging Multi-Mode reader (Biotek) at time zero and 72 h post Matrigel encapsulation. Image analysis was carried out using ImageJ by measuring the diameter of the invasive area. The degree of cell invasion into the Matrigel was measured for six replicate wells normalizing to each initial spheroid diameter at time-zero and the data plotted as a mean ratio for three biological repeats. 3D migration assays were similarly performed as previously described[58] with some modifications. In brief, flat-bottomed 96-well plates (Falcon) were coated with 2.5 μg per 50μl laminin per well (Thermo Fisher) in sterile water. Once coating was complete, a total of 200 μl per well of culture medium was added to each well. A total of 100 μl medium was removed from ULA 96-well round-bottomed plates containing neurospheres of ~200μm in diameter and the remaining medium including the neurosphere were transferred into the pre-coated plates. Images were obtained using the Cytation 5 Cell Imaging Multi-Mode reader (Biotek) at time zero and 72 h after Matrigel encapsulation. Image analysis was carried out using ImageJ by measuring the diameter of the invasive area. The degree of cell migration on the laminin was measured for six replicate wells normalizing to each spheroid time zero diameter and the data plotted as a mean ratio for three biological repeats.

Neuron–glioma co-culture EdU incorporation assay. For EdU incorporation assays, coverslips were prepared as described above. Again, at DIV 5, glioma cells were added to the neuron cultures. Forty-eight hours after addition of glioma cells,

slides were treated with 10 μM EdU with or without 10 μM NBQX (Tocris). Cells were fixed after an additional 24 h using 4% PFA and stained using the Click-iT EdU kit and protocol (Invitrogen). Proliferation index was then determined by quantifying percentage of EdU labelled glioma cells (identified by $EdU^+/nestin^+$) over total number of glioma cells using confocal microscopy.

Human electrocorticography, electrode localization and data analyses. All human electrocorticography data were obtained passively from adult study participants undergoing intraoperative brain mapping for surgical resection by co-author S.H.-J. Each participant was recruited from a prospective registry of adults aged 18–85 with newly diagnosed frontal, temporal, and parietal IDH-wild type high-grade gliomas. Informed consent for this study was obtained in accordance with the University of California, San Francisco (UCSF) institutional review board (IRB) for human research (UCSF CHR 17-23215). Subjects with tumors projecting to the cortical surface and at least three electrocorticography channels overlaying healthy-appearing brain (as determined by absence of FLAIR signal abnormality and absence of T1 post-gadolinium enhancement) were selected for analysis. Intraoperative photographs with and without subdural electrodes present were used to localize each electrode contact. Images were registered using landmarks from gyral anatomy and vascular arrangement to preoperative T_1- and T_2-weighted MRI scans. Tumour boundaries were localized on MRI scans and electrodes within 10 mm of necrotic tumour core tissue were identified as 'tumour' contacts. Electrodes overlying the hypointense core of the tumour were identified as 'core'; electrodes extending from the contrast enhancing rim extending to the edge of FLAIR were considered 'infiltrative margin'; and electrodes completely outside of any T_1 after gadolinium or FLAIR signal abnormality were considered 'healthy'.

Electrocorticographic signals were acquired during a three-minute resting-state period after stopping the administration of anaesthetics and the patient was judged to be alert and awake. Post-operative videos were re-analysed to ensure all data were collected in true resting state. Recordings were acquired at 4,800 Hz and downsampled to 1,200 Hz during the initial stages of processing. Channels with excessive noise artefacts were visually identified and removed. After the rejection of artefactual channels, data were referenced to a common average, high-pass filtered at 0.1 Hz to remove slow drift artefacts, and band-pass-filtered between 70 and 110 Hz using a 300-Order FIR filter to focus the analyses on the high-gamma band range, which is strongly related to local mean population spiking rates. High-gamma band power was then calculated using the square of the Hilbert transform on the filtered data. High-gamma band power was then averaged across the resting-state time series, yielding a single measure of neural responsivity for each electrode contact. High-gamma band power levels were then compared between tumour and non-tumour channels using independent samples *t*-tests separately for each patient.

Statistical analyses. Statistical tests were conducted using Prism (GraphPad) software unless otherwise indicated. Gaussian distribution was confirmed by the Shapiro–Wilk normality test. For parametric data, unpaired two-tailed Student's *t*-tests or one-way ANOVA with Tukey's post hoc tests to examine pairwise differences were used as indicated. Paired two-tailed Student's *t*-tests were used in the case of same cell experiments (as in electrophysiological recordings). For non-parametric data, a two-sided unpaired Mann–Whitney test was used as indicated, or a one-tailed Wilcoxon matched-pairs signed rank test was used in the case of same-cell experiments. Two-tailed log rank analyses were used to analyse statistical significance of Kaplan–Meier survival curves. For input–output curve comparison, nonlinear regression fits were compared using the extra-sum-of-squares *F*-test to compare separate versus individual best-fit models between datasets. A level of $P < 0.05$ was used to designate significant differences. On the basis of the variance of xenograft growth in control mice, we used at least three mice per genotype to give 80% power to detect an effect size of 20% with a significance level of 0.05. For all mouse experiments, the number of independent mice used is listed in figure legend.

Reporting summary. Further information on research design is available in the Nature Research Reporting Summary linked to this article.

Data availability

RNA sequencing of single-cell patient derived xenografts is available on Gene Expression Omnibus (GEO) under accession GSE134269. All other data are available in the article, source data, or from the corresponding author upon reasonable request.

Code availability

Custom code created will be available on GitHub upon request.

40. Yizhar, O., Fenno, L. E., Davidson, T. J., Mogri, M. & Deisseroth, K. Optogenetics in neural systems. *Neuron* **71**, 9–34 (2011).
41. Picelli, S. et al. Full-length RNA-seq from single cells using Smart-seq2. *Nat. Protoc.* **9**, 171–181 (2014).
42. Tirosh, I. et al. Single-cell RNA-seq supports a developmental hierarchy in human oligodendroglioma. *Nature* **539**, 309–313 (2016).
43. Butler, A., Hoffman, P., Smibert, P., Papalexi, E. & Satija, R. Integrating single-cell transcriptomic data across different conditions, technologies, and species. *Nat. Biotechnol.* **36**, 411–420 (2018).
44. Lin, G. L. et al. Non-inflammatory tumor microenvironment of diffuse intrinsic pontine glioma. *Acta Neuropathol. Commun.* **6**, 51 (2018).
45. Qin, E. Y. et al. Neural precursor-derived pleiotrophin mediates subventricular zone invasion by glioma. *Cell* **170**, 845–859.e819 (2017).
46. Rueden, C. T. et al. ImageJ2: ImageJ for the next generation of scientific image data. *BMC Bioinformatics* **18**, 529 (2017).
47. Schindelin, J. et al. Fiji: an open-source platform for biological-image analysis. *Nat. Methods* **9**, 676–682 (2012).
48. Schneider, C. A., Rasband, W. S. & Eliceiri, K. W. NIH Image to ImageJ: 25 years of image analysis. *Nat. Methods* **9**, 671–675 (2012).
49. Pietzsch, T., Preibisch, S., Tomancák, P. & Saalfeld, S. ImgLib2—generic image processing in Java. *Bioinformatics* **28**, 3009–3011 (2012).
50. Wu, D. et al. Postsynaptic synaptotagmins mediate AMPA receptor exocytosis during LTP. *Nature* **544**, 316–321 (2017).
51. Guizar-Sicairos, M., Thurman, S. T. & Fienup, J. R. Efficient subpixel image registration algorithms. *Opt. Lett.* **33**, 156–158 (2008).
52. Achanta, R. et al. SLIC superpixels compared to state-of-the-art superpixel methods. *IEEE Trans. Pattern Anal. Mach. Intell.* **34**, 2274–2282 (2012).
53. Pnevmatikakis, E. A. et al. Simultaneous denoising, deconvolution, and demixing of calcium imaging data. *Neuron* **89**, 285–299 (2016).
54. van der Walt, S. et al. scikit-image: image processing in Python. *PeerJ* **2**, e453 (2014).
55. Kawahara, Y., Ito, K., Sun, H., Kanazawa, I. & Kwak, S. Low editing efficiency of GluR2 mRNA is associated with a low relative abundance of ADAR2 mRNA in white matter of normal human brain. *Eur. J. Neurosci.* **18**, 23–33 (2003).
56. Sobolevsky, A. I., Rosconi, M. P. & Gouaux, E. X-ray structure, symmetry and mechanism of an AMPA-subtype glutamate receptor. *Nature* **462**, 745–756 (2009).
57. Vinci, M., Box, C. & Eccles, S. A. Three-dimensional (3D) tumor spheroid invasion assay. *J. Vis. Exp.* **99**, 52686 (2015).
58. Vinci, M., Box, C., Zimmermann, M. & Eccles, S. A. Tumor spheroid-based migration assays for evaluation of therapeutic agents. *Methods Mol. Biol.* **986**, 253–266 (2013).

Acknowledgements We gratefully acknowledge support from the National Institutes of Health (NIH) Director's Common Fund (DP1 NS111132 to M.M.), National Institute of Neurological Disorders and Stroke (R01 NS092597 to M.M., K08 NS110919 to S.H.-J.), National Cancer Institute (F31 CA200273 to H.S.V.), National Institutes of Mental Health (P50 MH086403 to R.C.M.), Michael Mosier Defeat DIPG Foundation (to M.M.), ChadTough Foundation (to M.M.), V Foundation (to M.M.), Department of Defense (NF140075 to M.M.), McKenna Claire Foundation (to M.M.), Alex's Lemonade Stand Foundation (to M.M.), The Cure Starts Now Foundation and DIPG Collaborative (to M.M.), Unravel Pediatric Cancer (to M.M.), N8 Foundation (to M.M.), Abbie's Army Foundation (to M.M.), Brantley's Project supported by Ian's Friends Foundation (to M.M.), Waxman Family Research Fund (to M.M.), Joey Fabus Childhood Cancer Foundation (to M.M.), Virginia and D.K. Ludwig Fund for Cancer Research (to M.M.), Bio-X Institute (to L.T.T. and A.C.G.), Maternal and Child Health Research Institute at Stanford (to M.M., A.C.G and H.S.V.), Anne T. and Robert M. Bass Endowed Faculty Scholarship in Pediatric Cancer and Blood Diseases (to M.M.), Cancer Research UK (to M.M.), Dr. Mildred Scheel Cancer Foundation (57406718 to M.A.), Damon Runyan Foundation (to K.R.T.), Sontag Foundation Distinguished Scientist Award (to M.L.S.), Howard Hughes Medical Institute (to A.R.), Klarman Cell Observatory (to A.R.), Dr. Miriam and Sheldon G. Adelson Medical Research Foundation (to D.E.B.), Chica and Heinz Schaller Research Foundation (to A.A.), Deutsche Forschungsgemeinschaft (AG 287/1-1 to A.A.), The Robert Wood Johnson Foundation (74259 RWJF to S.H.-J.). We thank S. Knemeyer for illustrations, and A. Olsen, S. Kakaizada and M. Shore for technical assistance.

Author contributions H.S.V. and M.M. designed, conducted, and analysed experiments. W.M. conducted electrophysiology experiments. L.N. and H.V. contributed to electron microscopy data acquisition and analyses. S.H.-J. performed intraoperative electrocorticography. D.B. conducted high-gamma frequency power computational analyses. D.S., M.L.S., A.R. and S.M.G. contributed to single-cell transcriptomic analyses. S.M.G. and M.A. contributed to synaptic puncta and tumour microtube confocal imaging, A.C.G. and L.T.T. contributed to optogenetic experiments. A.A. and D.E.B. provided the GluA2 dominant-negative construct. A.P., K.R.T. and P.J.W. contributed to in vitro and in vivo data collection and analyses. C.E. contributed to quantitative imaging analyses. R.C.M., D.E.B., S.M.G., W.M., H.S.V. and M.M. contributed to manuscript editing. H.S.V. and M.M. wrote the manuscript. M.M. conceived of the project and supervised all aspects of the work.

Competing interests M.M. is an SAB member of Cygnal Therapeutics. A.R. is a founder and equity holder of Celsius Therapeutics and an SAB member of ThermoFisher Scientific, Neogene Therapeutics and Syros Pharmaceuticals.

Additional information

Supplementary information is available for this paper at https://doi.org/10.1038/s41586-019-1563-y.

Correspondence and requests for materials should be addressed to M.M.

Peer review information *Nature* thanks Andres Barria, Michael Taylor and the other, anonymous, reviewer(s) for their contribution to the peer review of this work.

Reprints and permissions information is available at http://www.nature.com/reprints.

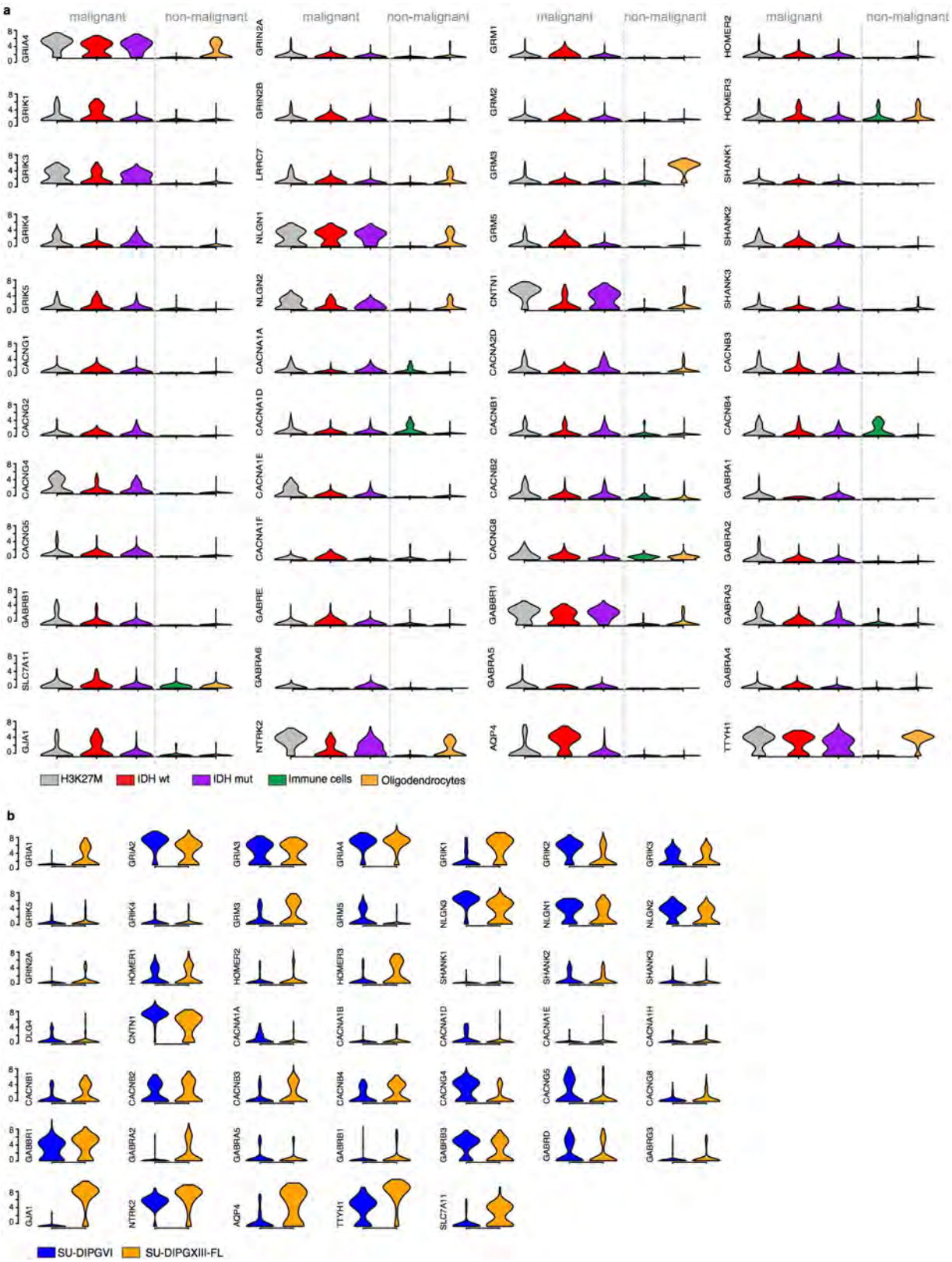

Extended Data Fig. 1 | Synaptic gene expression in single cell primary glioma and patient-derived xenografts. a, Primary human biopsy single-cell transcriptomic data illustrating synapse associated and ion channel gene expression in H3K27M^{+} DMG (grey, $n = 2,259$ cells, 6 study participants), wild-type IDH adult high-grade glioma (red, $n = 599$ cells, 3 participants), IDH-mutant adult high-grade glioma (purple, $n = 5,096$ cells, 10 particpants) malignant cells, and tumour-associated, non-malignant immune cells (green; $n = 96$ cells, 5 participants) and oligodendrocytes (yellow; $n = 232$ cells). **b**, As in **a** for single-cell transcriptomic analysis of H3K27M^{+} DMG xenograft models (SU-DIPG-VI, blue; and SU-DIPG-XIII-FL, yellow) illustrating broad synaptic gene expression similar to that found in primary DMG tissue samples as shown in Fig. 1a. For each individual violin plot, the *y* axis represents $\log_2$(transcripts per million), and the *x* axis represents number of individual cells with indicated expression value.

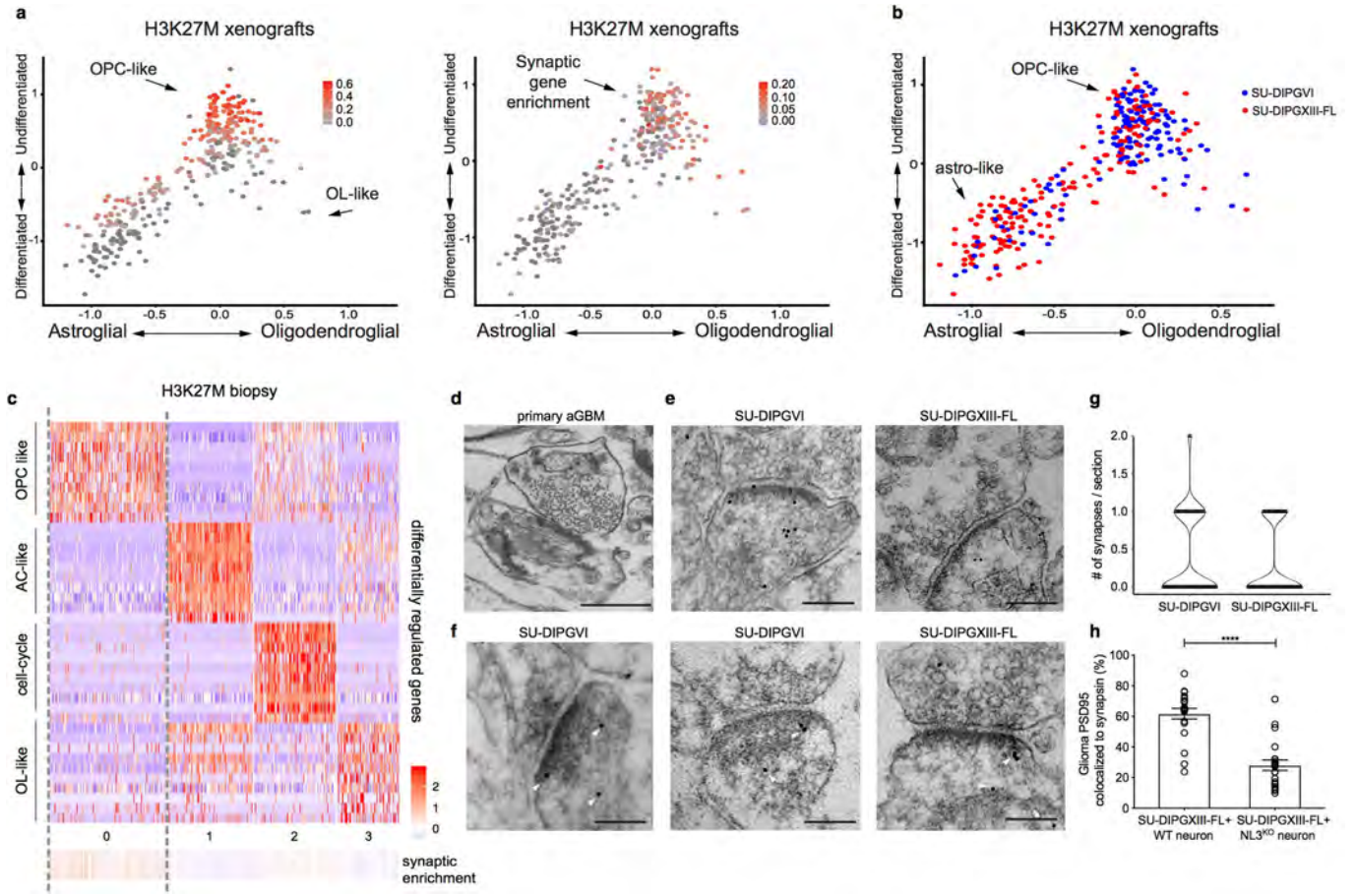

Extended Data Fig. 2 | Synaptic gene expression and structural synapses in glioma. a, Plot of the lineage (*x* axis) and stemness (*y* axis) scores for H3K27M^{+} DIPG malignant single cells (dots) sorted from patient-derived glioma xenograft models (SU-DIPG-VI and SU-DIPG-XIII-FL). Overlay of grey–red enrichment score indicates relative score for OPC-like genes (left) and synapse-related genes (right; $n = 335$ cells, 4 mice; Pearson correlation rho = 0.57, $P < 0.0001$). **b**, Plot of the lineage versus stemness scores for H3K27M^{+} DIPG malignant single cells in **a**, coloured by xenograft model. Red denotes SU-DIPG-XIII-FL, blue denotes SU-DIPG-VI. Although each xenograft model clearly contains cells across all lineages, SU-DIPG-XIII-FL has a prominent astrocyte-like cell population, whereas SU-DIPG-VI has a prominent OPC-like population. **c**, Unbiased principal component analysis of single-cell gene expression from an individual patient primary biopsy sample of H3K27M^{+} glioma (BCH869) reveals cellular clusters that resemble proliferating cells (cell-cycle), OPCs (OPC-like), astrocytes (AC-like) and oligodendrocytes (OL-like). Synaptic gene enrichment for individual cells shown below and co-localizes in the OPC-like cluster. **d**, Electron microscopy images of primary adult glioblastoma tumour sample illustrating clear synaptic structure. Scale bars, 500 μm. **e**, Original (non-pseudo-coloured) immuno-electron microscopy images shown in Fig. 1c. **f**, Additional examples of neuron–glioma synapses identified by immuno-electron microscopy in patient-derived xenografts of SU-DIPG-VI and SU-DIPG-XIII-FL ($n = 3$ mice per group). Arrowheads indicate immuno-gold particle labelling of GFP. Scale bars, 200 μm. **g**, Quantification of neuron–glioma synaptic structures in SU-DIPG-VI ($n = 101$ sections) and SU-DIPG-XIII-FL ($n = 104$ sections) xenografts. For each individual violin plot, *y* axis represents number of identified unambiguous neuron–glioma synapses in each section, *x* axis represents number of individual cells with indicated value. **h**, Quantification of colocalized postsynaptic glioma-derived PSD95–RFP with presynaptic synapsin in co-cultures of SU-DIPG-XIII-FL glioma cells with wild-type or *Nlgn3*^{KO} neurons ($n = 21$ cells, 10 coverslips per group). Data are mean ± s.e.m. ****$P < 0.0001$, two-sided Mann–Whitney test.

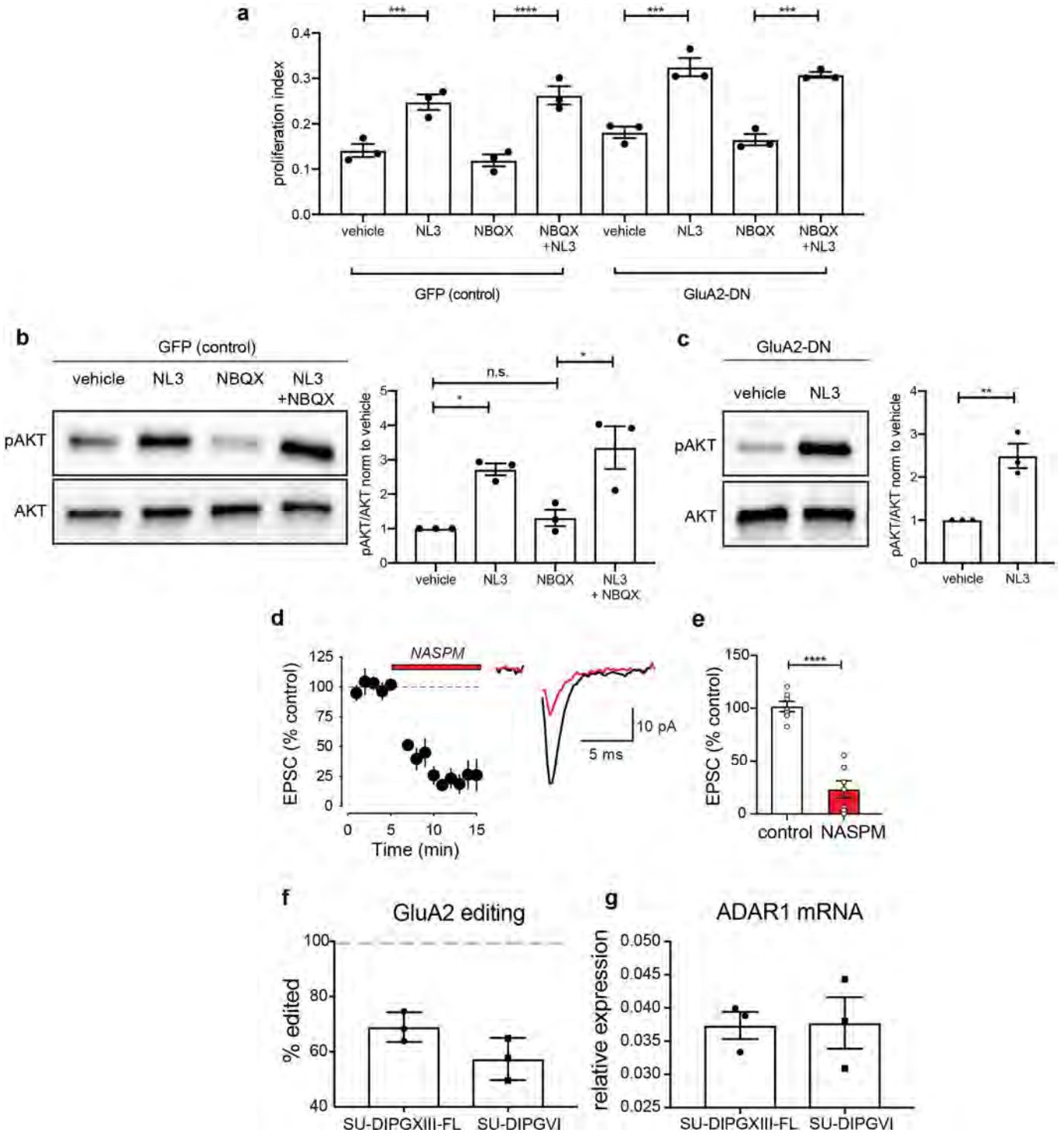

Extended Data Fig. 3 | Mitogenic effects of NLGN3 are independent from AMPAR signalling and properties of glioma AMPARs. **a**, Proliferative response of GFP (control) and GluA2-DN-expressing glioma cells after 24 h exposure to soluble extracellular NLGN3 (100 nM) in the presence and absence of AMPAR blocker NBQX (10 μM). **b**, Left, western blot analysis of phosphorylated-AKT (Ser473; pAKT) and total AKT in GFP (control) glioma cells in response to 5-min exposure to NLGN3 (100 nM) in the presence and absence of 10 μM NBQX. Right, quantitative analysis of the ratio of pAKT/AKT normalized to vehicle. **c**, Left, western blot analysis of pAKT and total AKT in GluA2-DN-expressing glioma cells in response to 5-min exposure to 100 nM NLGN3. Right, quantitative analysis of the ratio of pAKT/AKT normalized to vehicle. **d**, Left, time course of evoked glioma cell EPSC block by 100 μM NASPM (red bar denotes duration; $n = 7$ cells, 5 mice). Right, representative trace before (black) and after (red) addition of NASPM. **e**, Quantification of data in **d**. **f**, Q/R editing efficiency of GluA2 subunit in SU-DIPG-XIII-FL and SU-DIPG-VI cells as measured by PCR and expressed as percentage edited. **g**, Expression of *ADAR1* (also known as *ADAR*), which encodes the enzyme responsible for Q/R editing of *GluA2* (also known as *GRIA2*) mRNA. mRNA expression shown relative to *ACTB* and measured by quantitative PCR. Analyses in **a**–**c**, **f**, **g** were calculated from three independent sets of cells. Data are mean ± s.e.m. $^{*}P < 0.01$, $^{**}P < 0.001$, $^{***}P < 0.001$, $^{****}P < 0.0001$, one-way ANOVA with Tukey's post hoc analysis (**a**, **b**), two-tailed unpaired Student's *t*-test (**c**) or two-tailed paired Student's *t*-test (**e**). n.s., not significant.

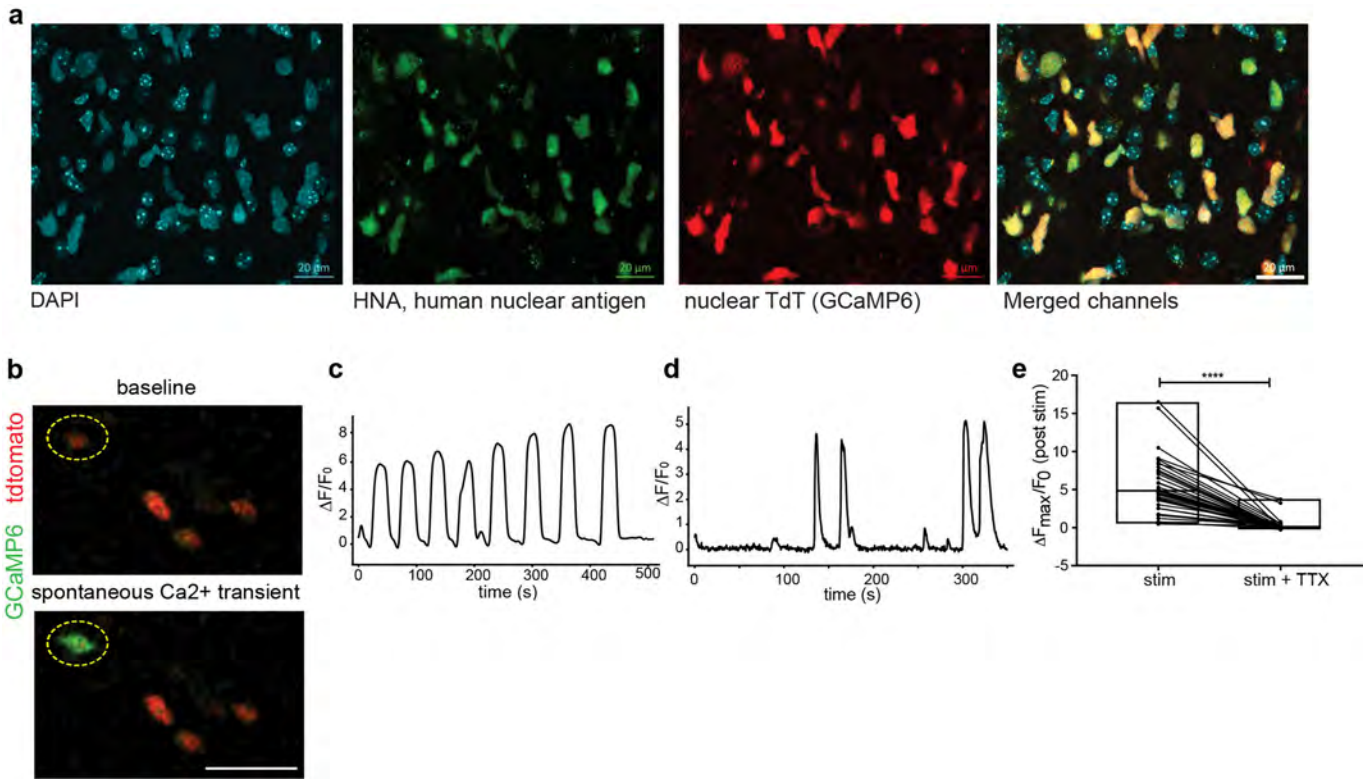

Extended Data Fig. 4 | Glioma xenograft calcium imaging with GCaMP6. a, Confocal micrographs of xenografted SU-DIPG-XIII-FL cells expressing GCaMP6s-tdTomato into the hippocampus, and stained with DAPI (blue), HNA (green), and tdTomato nuclear tag (red). Merged image illustrates specificity of tdTomato tag to HNA^+ cells. Scale bars, 20 μm. Immunostaining independently replicated in three mice. **b**, Spontaneous calcium transients in SU-DIPG-VI xenograft visualized by two-photon in situ calcium imaging ($n = 5$ mice). Representative frames shown. Red denotes glioma tdTomato nuclear tag; green denotes GCaMP6s. Scale bar, 50 μm. See also Supplementary Video 1. **c**, Trace of normalized GCaMP6s intensity over time in an individual xenografted glioma (SU-DIPG-VI) cell exhibiting an oscillatory spontaneous transient. Results were replicated across $n = 3$ mice. **d**, As in **c**, trace of normalized GCaMP6s intensity over time in an individual xenografted glioma (SU-DIPG-XIII-FL) cell exhibiting a less regular spontaneous transient. This type of transient is more frequently observed in glioma xenografts. Results were replicated across $n = 3$ mice. **e**, Individual xenografted glioma (SU-DIPG-XIII-FL) cellular responses to axonal stimulation before and after application of 0.5 μM TTX as measured by GCaMP6s intensity ($n = 40$ cells, 4 mice). Data are mean ± s.e.m. $^{****}P < 0.0001$, one-tailed Wilcoxon matched-pairs signed rank test.

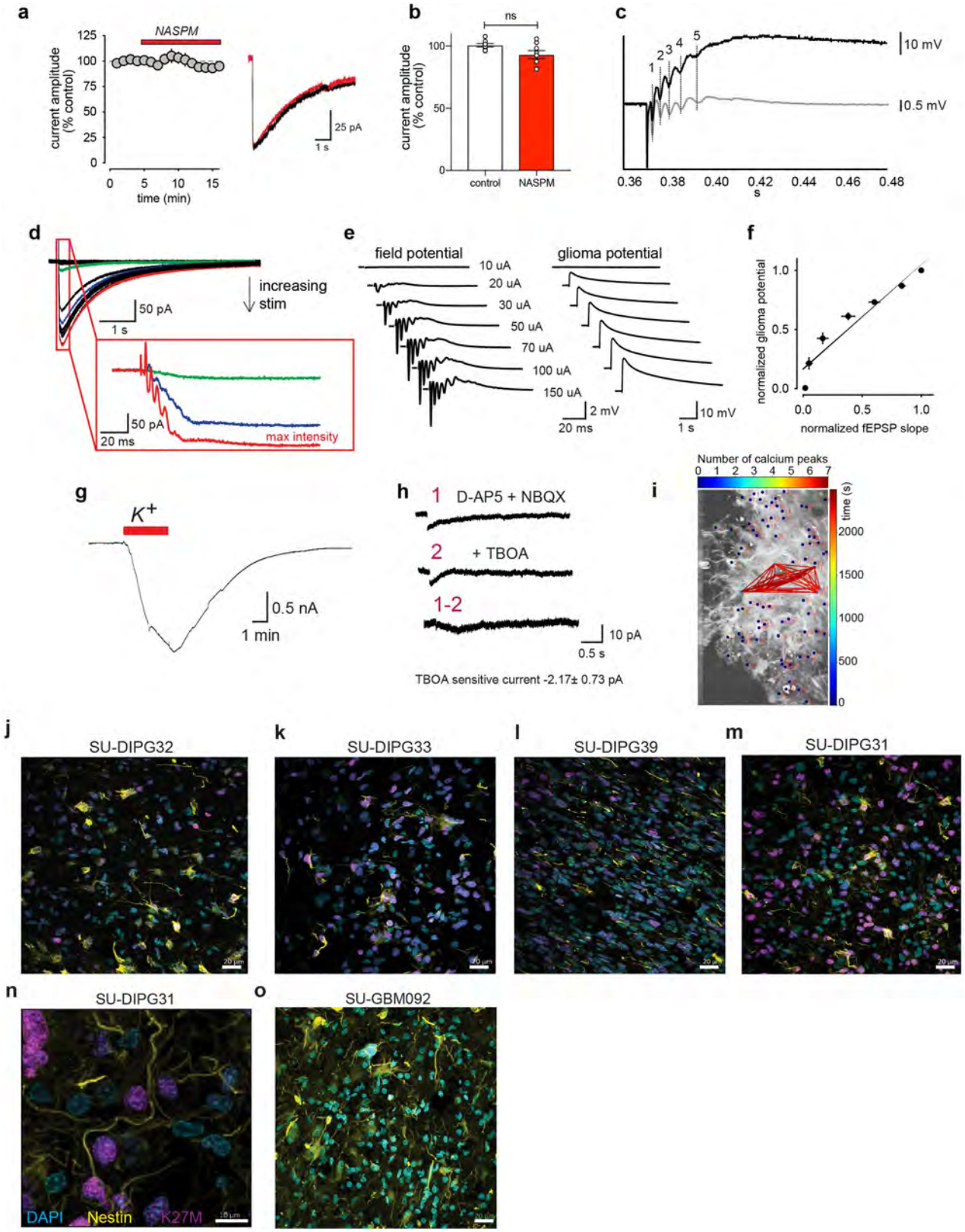

Extended Data Fig. 5 | See next page for caption.

Extended Data Fig. 5 | Prolonged glioma currents and paediatric glioma tumour microtubes. a, Left, time course of prolonged current block by 100 μM NASPM (red bar denotes duration of NASPM application; $n = 8$ cells, 5 mice). Data are mean ± s.e.m. Right, representative traces of evoked prolonged current (block) unaffected by NASPM (red). **b**, Quantification of data in **a**. Data are mean ± s.e.m; ns, not significant (two-tailed paired Student's *t*-test). **c**, Alignment of phase-locked simultaneous recording of glioma prolonged potential with the field potential of firing neuronal population. **d**, Representative prolonged current traces with increasing stimulation intensity. Red denotes maximum intensity; blue and green denote intermediate intensities. Magnified view illustrates distinct spike-like waveforms consistent with responses to neuronal population firing. **e**, Relationship of extracellular field potential to magnitude of prolonged current (SU-DIPG-XIII-FL xenograft) illustrated by simultaneous field potential (fEPSP) and whole-cell glioma current-clamp recordings. **f**, Prolonged glioma potential amplitudes versus slope of fEPSPs elicited by electrical stimulation (10, 20, 30, 50, 70, 100 and 150 μA; $R^2 = 0.92$; $n = 14$ cells or fields across 4 mice for each, except $n = 11$ cells or fields across 3 mice for 30 μA). **g**, Representative trace of potassium (K^+)-induced prolonged current in SU-DIPG-XIII-FL xenografts ($n = 9$ cells, 2 mice). **h**, Effect of TBOA on prolonged current in glioma (SU-DIPG-XIII-FL) ($n = 5$ cells, 2 mice). (1) Representative trace of residual current left after application of d-AP5 and NBQX in prolonged response to stimulation. d-AP5 and NBQX are likely to reduce the prolonged current owing to the effect on CA1 pyramidal neurons, not through direct effect on the glioma cells themselves; (2) representative trace of residual current after trace 1 was then treated with glutamate transporter blocker 200 μM TBOA; (1 − 2) subtraction of trace 2 from trace 1 reveals a 2 pA current that can be accounted for by glutamate transporters. It should be noted that a small residual current remains. **i**, Synchronicity analysis of calcium peaks in glioma cells in Fig. 3 shown over the course of 10 min. Red lines indicate cells synchronized with one another at various time points during indicated period. **j**–**o**, Confocal micrographs of primary human glioma tissue samples illustrate density and length of nestin-immunopositive tumour microtubes. **j**–**n**, Primary human tissue samples of paediatric $H3K27M^+$ DIPG, sampled at the time of autopsy. **o**, Analysis of primary tissue sample from an adult glioblastoma (SU-GBM092) illustrates the similarity of paediatric glioma to adult glioma. For all images, blue denotes DAPI; yellow denotes nestin; magenta denotes H3K27M (tumour-specific antigen). Scale bars, 20 μm (**j**–**m**, **o**), or 10 μm (**n**). Data independently replicated in three sections per sample.

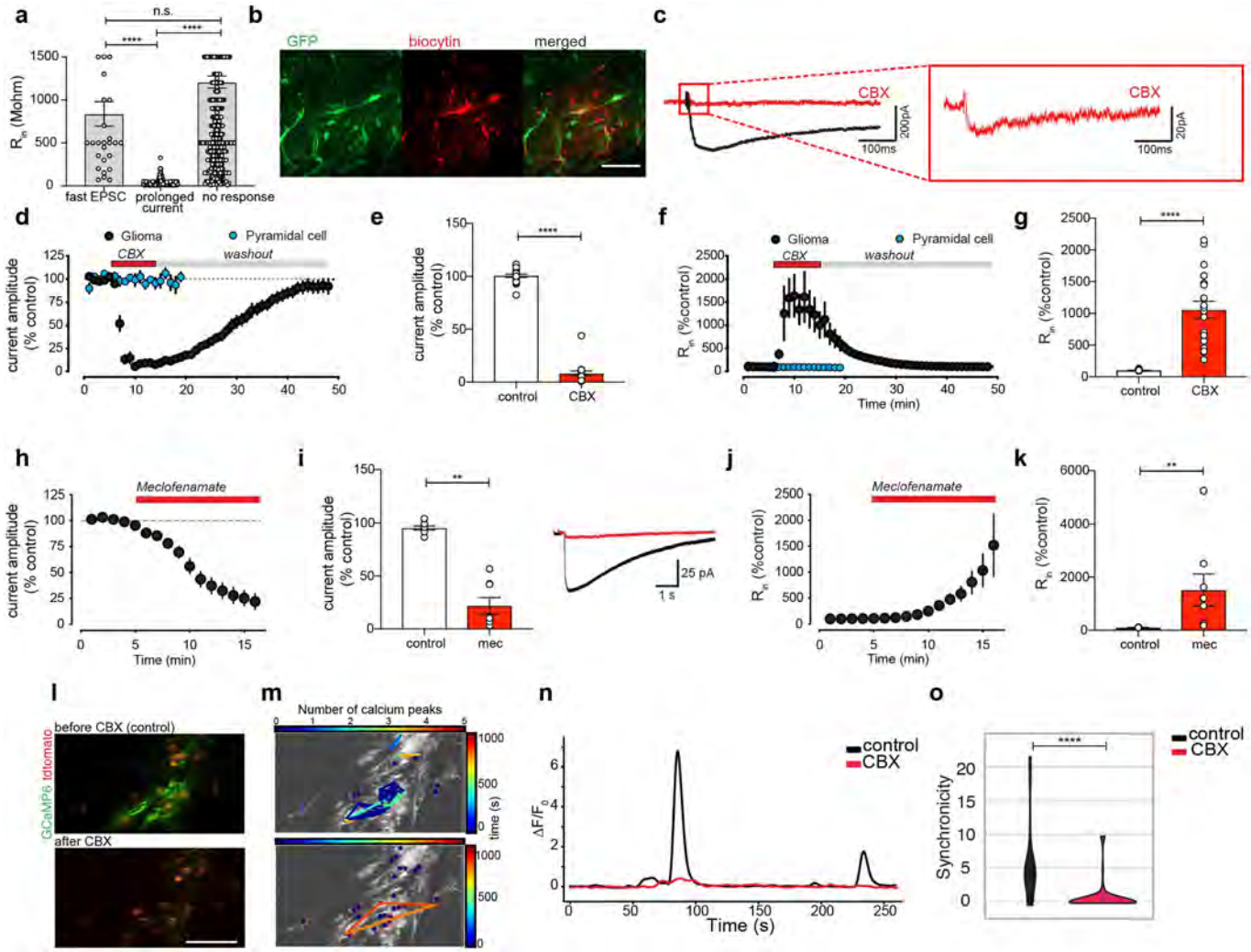

Extended Data Fig. 6 | Prolonged currents in paediatric glioma amplified by gap junction coupling. a, Input resistance of non-responding and depolarizing cells ($n = 29$ fast EPSCs, $n = 247$ prolonged currents, $n = 319$ no response, data points above 1500 MΩ have been left off graph for clarity). **b**, Biocytin dye-filling illustrates coupling of xenografted glioma cells that exhibit prolonged currents ($n = 7$ slices, 2 mice). Red denotes streptavidin–biocytin; green denotes GFP. Scale bar, 100 μm. **c**, Prolonged currents in glioma markedly decreased by 100 μM CBX. Red box highlights magnified view of representative trace to illustrate residual slow current after application of CBX. **d**, Time course of prolonged current in glioma cell (black) and pyramidal neuron EPSC (blue) responses to the addition of CBX with subsequent washout of inhibitor (red bar denotes duration of CBX application; $n = 6$ glioma cells, 6 mice; $n = 5$ neurons, 2 mice). **e**, Quantification of the drop in current amplitude after addition of CBX ($n = 19$ cells, 11 mice; data also shown in Fig. 3g). **f**, Input resistance of cells in **d** in response to CBX. **g**, Quantification of data in **f** ($n = 19$ cells, 11 mice). **h**, Time course of prolonged current in glioma in response to addition of 100 μM meclofenamate (red bar denotes duration; $n = 8$ cells, 3 mice). **i**, Left, quantification of data in **h**; data also shown in Fig. 3g. Right, representative traces illustrating decrease in prolonged current amplitude after addition of meclofenamate (red). **j**, Input resistance of cells in **h** in response to addition of meclofenamate ($n = 8$ cells, 3 mice). **k**, Quantification of data in **j**. **l**, Representative frames from two-photon calcium imaging of in situ SU-DIPG-XIII-FL glioma xenografts illustrating spontaneous transients before (top) or after (bottom) addition of CBX. Red denotes tdTomato nuclear tag in glioma cells; green denotes GCaMP6s. Scale bar, 50 μm. Results replicated across three mice. **m**, Synchronicity analyses of spontaneous calcium transients before (top) or after (bottom) addition of CBX. **n**, Representative trace of GCaMP6s peak intensity over time in a single cell before (black) and after (red) addition of CBX ($n = 3$ mice). **o**, Synchronicity scores of individual cells within glioma xenografts before and after addition of CBX ($n = 164$ cells, 3 mice). *y* axis represents synchronicity score; *x* axis represents number of cells with specific score. Data are mean ± s.e.m. (**a**, **d**–**k**). $^{**}P < 0.01$, $^{****}P < 0.0001$, one-way ANOVA with Tukey's post hoc analysis (**a**) or one-tailed Wilcoxon matched-pairs signed rank test (**e**, **g**, **i**, **k**, **o**).

a

pHGG model	fast EPSC	prolonged current	no response	total
SU-DIPGVI	29	23	243	295
SU-DIPGXIII	3	165	40	208
SU-pcGBM2	0	58	20	78
SU-DIPG25	4	5	53	62
total	36	251	356	643

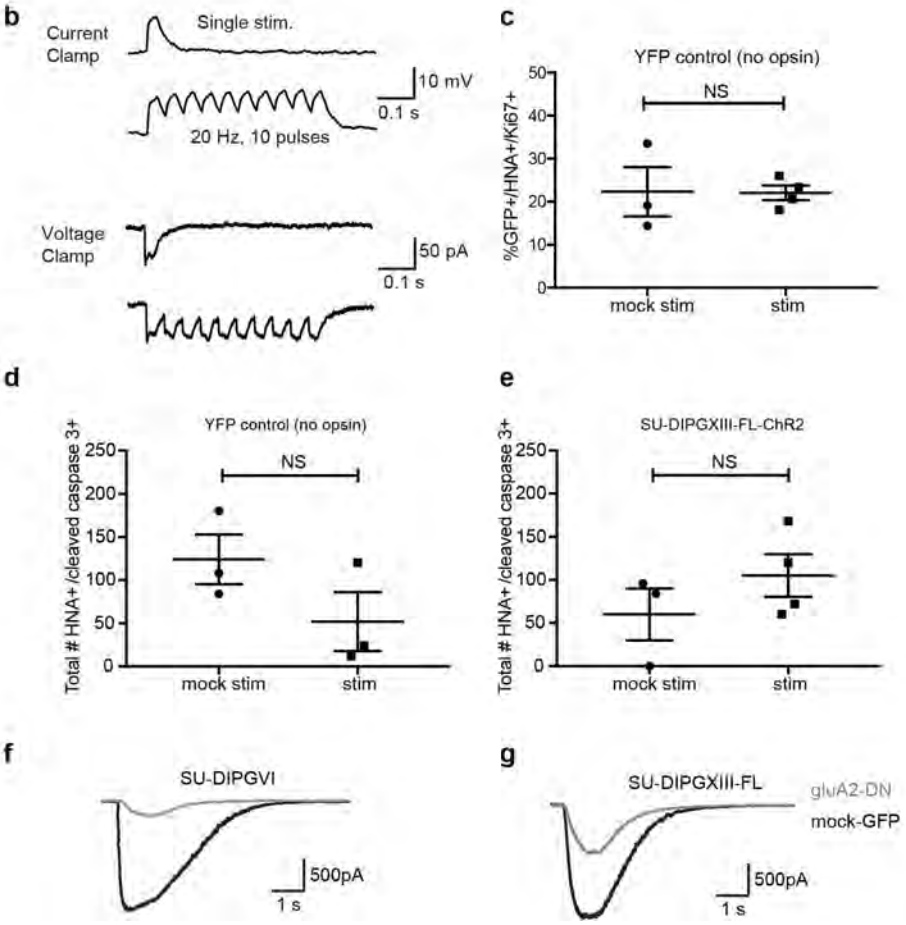

Extended Data Fig. 7 | Heterogeneity of glioma cell electrophysiological response and validation of ChR2 and GluA2-DN function in glioma. **a**, Electrophysiological responses by patient-derived pediatric high-grade glioma (pHGG) model. Number of whole-cell patch-clamp recordings from glioma cells in xenografted hippocampal slices categorized by electrophysiological response to axonal electrical stimulation. **b**, Demonstration of depolarizing inward current in SU-DIPG-XIII-FL-ChR2 cells in response to single stimulation and 20 Hz pulses of blue light as measured in current clamp (top) and voltage clamp (bottom). **c**, Proliferation index of xenografted SU-DIPG-XIII-FL-YFP control glioma cells (no opsin expressed) in response to blue-light or mock stimulation as measured by the proportion of GFP^+/HNA^+ cells expressing Ki67 24 h after five optogenetic stimulation sessions ($n = 3$ mice, mock stim; $n = 4$ mice, stim). **d**, Quantification of cleaved caspase-3 in xenografted SU-DIPG-XIII-FL-YFP control glioma cells in response to blue-light or mock stimulation as measured by total number of HNA^+ cells co-labelled with cleaved caspase-3 ($n = 3$ mice per group). **e**, As in **d**, but for xenografted SU-DIPG-XIII-FL-ChR2 glioma cells ($n = 3$ mice, mock stim; $n = 4$ mice, stim). **f**, **g**, Validation of GluA2-DN-expressing construct. Representative traces of whole-cell voltage-clamp recording of wild-type (black) and GluA2-DN-expressing (grey) SU-DIPG-VI (**f**) or SU-DIPG-XIII-FL (**g**) cells in response to 500μM (*S*)-AMPA ($n = 6$ cells for each). SU-DIPG-XIII-FL cells are unable to homogeneously express the dominant construct, and therefore may be gap junction-coupled to wild-type GluA2-expressing cells, which may account for the remaining current in the illustrated trace (**g**). Incorporation of the GluA2-DN construct thus results in abrogated AMPAR-dependent depolarization. Data are mean ± s.e.m. (**c**–**e**). NS, not significant (two-tailed unpaired Student's *t*-test).

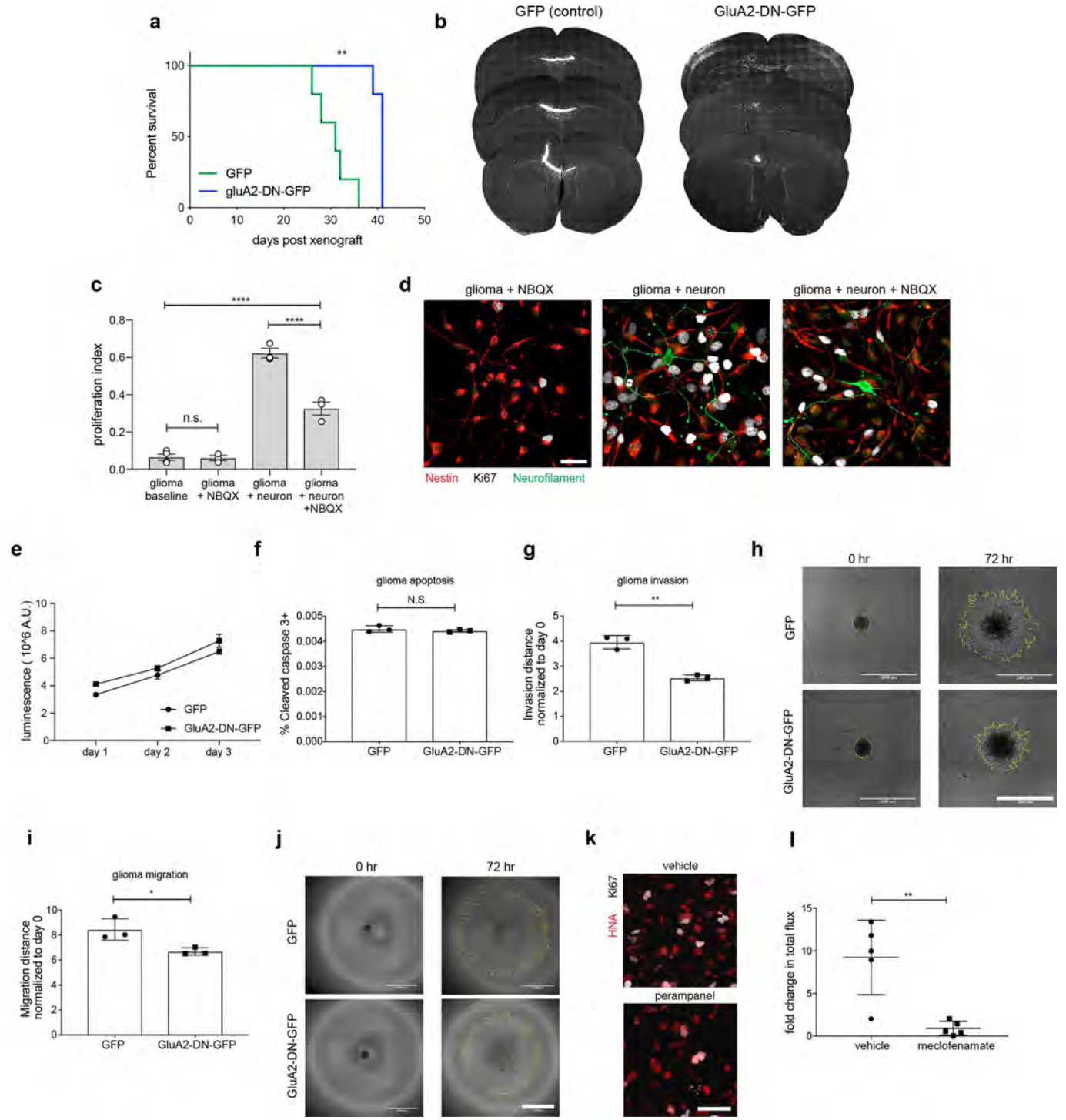

Extended Data Fig. 8 | See next page for caption.

Extended Data Fig. 8 | Glioma AMPAR function in vitro, in co-culture and in vivo. a, Kaplan–Meier survival curves of a second cohort of mice orthotopically xenografted with control GFP-only or GluA2-DN-GFP-overexpressing cells (SU-DIPG-XIII-P* xenograft model; $n = 5$ mice per group). **b**, Representative serial coronal sections of mouse brains bearing SU-DIPG-XIII-FL xenografts expressing either control GFP construct (left) or GluA2-DN-GFP construct (right). Grey denotes MBP; white denotes glioma-GFP. **c**, Proliferation indices of SU-DIPG-XIII-FL cells at baseline in neuronal medium, in response to 10 μM NBQX, in co-culture with neurons, or in co-culture with neurons in the presence of 10 μM NBQX ($n = 3$ biological replicates per group, except $n = 4$ for baseline). **d**, Representative images of neuron–glioma co-cultures in the presence and absence of NBQX. Green denotes neurofilament (neuronal processes); red denotes nestin (glioma cell processes); white denotes Ki67. Scale bar, 50 μm. **e**, In vitro growth analysis of glioma cells expressing control GFP or GluA2-DN-GFP monitored over 3 days. **f**, In vitro apoptosis analysis of glioma cells expressing control GFP or GluA2-DN-GFP as measured by percentage of total cells co-stained with cleaved caspase-3. **g**, 3D Matrigel invasion assay in control GFP-expressing and GluA2-DN-GFP-expressing SU-DIPG-XIII-FL cells 72 h after seeding. **h**, Representative images of data in **g** at time 0 h (left) and 72 h (right) in control GFP-expressing (top) and GluA2-DN-GFP-expressing cells (bottom). Scale bars, 1,000 μm. **i**, 3D migration in control GFP-expressing and GluA2-DN-GFP-expressing SU-DIPG-XIII-FL cells 72 h after seeding. **j**, Representative images of data in **i** at time 0 h (left) and 72 h (right) in control GFP-expressing (top) and GluA2-DN-GFP-expressing cells (bottom). Scale bars, 1,000 μm. **k**, Representative confocal micrographs illustrating proliferating SU-DIPG-VI cells in vehicle or perampanel-treated mice ($n = 8$ mice per group). Red denotes human nuclei (HNA); white denotes Ki67. Scale bar, 50 μm. **l**, IVIS bioluminescence analysis of overall tumour growth in SU-DIPG-XIII-FL xenografts treated with vehicle or meclofenamate over a two-week period ($n = 5$ mice per group). Data represented as fold change in total flux. Data shown are mean ± s.e.m. (**c**, **e**–**g**, **i**, **l**). For analyses in **d**–**j**, $n = 3$ biological replicates. $^{*}P < 0.05$, $^{**}P < 0.01$, $^{****}P < 0.0001$, two-tailed log rank analyses (**a**), one-way ANOVA with Tukey's post hoc analysis (**c**), or two-tailed unpaired Student's *t*-test (**f**, **g**, **i**, **l**).

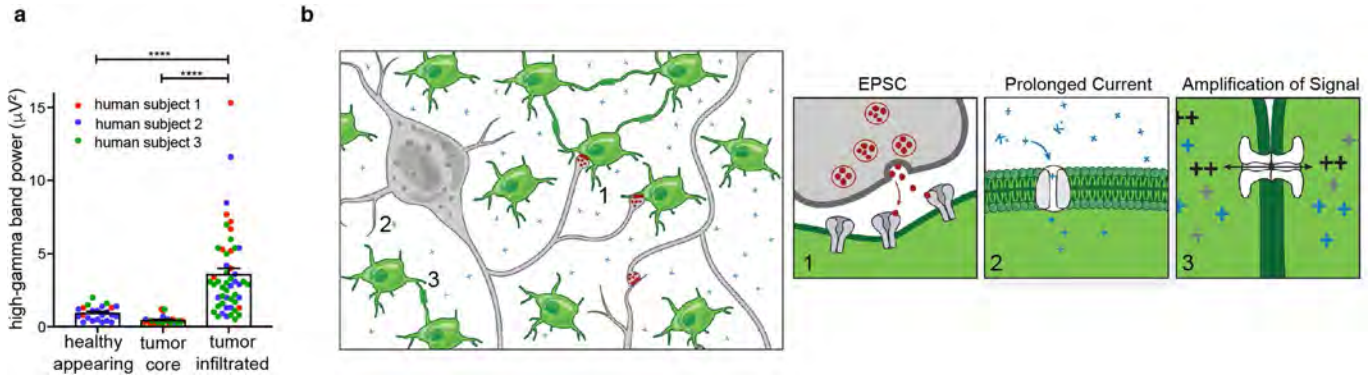

Extended Data Fig. 9 | Hyperexcitability in the glioma microenvironment and working model of neuron–glioma interactions in the tumour microenvironment. a, Individual channel electrocorticography signals (mean high-gamma frequency-filtered power) in each of healthy-appearing, tumour core, and tumour-infiltrated brain ($n = 23$, 29 and 51 total channels, respectively) across three human subjects, as in Fig. 5a, b. Data shown are mean ± s.e.m. ****$P < 0.0001$, one-way ANOVA with Tukey's post hoc analysis. **b**, Working model of glioma integration into neural circuity, with hyperexcitability of neurons (grey) exacerbating activity-dependent mechanisms of glioma (green) growth. (1) neuron-to-glioma synapses (synaptic vesicles in red; AMPARs in grey); (2) inward potassium (K^+) current (blue; potassium channel in grey); (3) gap junction (white) coupling in glioma amplifies current.

Extended Data Table 1 | Characteristics of human subjects and patient-derived high-grade glioma cell cultures, xenograft models and primary tissue samples

Culture ID	Tumor type, location and grade	Age at diagnosis (years)	Patient sex	Histone-3 mutational status	Other genomic character-istics	Timepoint tissue obtained	Prior therapy	Survival (months)
SU-pcGBM2	Pediatric cortical glioblastoma; frontal lobe; WHO grade IV	15	M	WT	P53 mutated EGFR amplified	Biopsy at diagnosis	none	21
SU-DIPGVI	DIPG; pons; WHO grade IV	7	F	H3.3K27M	N/A	Early postmortem autopsy	XRT; vorinostat	6
SU-DIPGXIII-P*	DIPG; pons; WHO grade IV	6	F	H3.3K27M	N/A	Early postmortem autopsy	XRT	4
SU-DIPGXIII-FL	DIPG; frontal lobe met; WHO grade IV	6	F	H3.3K27M	N/A	Early postmortem autopsy	untreated	4
SU-DIPG25	DIPG; pons; WHO grade IV	5 (at death)	F	H3.3K27M	N/A	Early postmortem autopsy	XRT	11
SU-DIPG31	DIPG; pons; WHO grade IV	18	M	H3.3K27M	N/A	Early postmortem autopsy	XRT; etoposide	N/A
SU-DIPG32	DIPG; pons; WHO grade IV	5	M	H3.1K27M	N/A	Early postmortem autopsy	XRT; avastin	N/A
SU-DIPG33	DIPG; pons; WHO grade IV	8	M	H3.1K27M	N/A	Early postmortem autopsy	XRT	N/A
SU-DIPG39	DIPG; pons; WHO grade IV	5 (at death)	M	H3.3K27M	N/A	Early postmortem autopsy	XRT	6
SU-GBM092	GBM; hemispheric; WHO grade IV	47	M	N/A	N/A	Early postmortem autopsy	Resection; XRT; TMZ	6
SF0047 (human subject 1)	GBM; left temporal lobe; WHO grade IV	57	M	N/A	Neg IDH1 R132H; MGMT unmeth-ylated	Resection at diagnosis	none	N/A
SF0109 (human subject 2)	GBM; left parietal lobe; WHO grade IV	63	M	N/A	Neg IDH1 R132H	Resection at diagnosis	none	N/A
SF0144 (human subject 3)	HGG; left temporal lobe; WHO grade III	74	M	N/A	Neg IDH1 R132H; ATRX WT	Resection at diagnosis	none	N/A

Note that SU-DIPG-XIII-P* and SU-DIPG-XIII-FL were tissue samples acquired from the same patient at autopsy; in this case the pontine tumour (P) received focal radiotherapy, whereas the frontal lobe (FL) tumour was an untreated metastasis from the primary pontine tumour to the frontal lobe. DIPG, diffuse intrinsic pontine glioma; GBM, glioblastoma; HGG, high-grade glioma; TMZ, temozolomide; WHO, World Health Organization; XRT, radiotherapy.

nature research

Corresponding author(s): Michelle Monje

Reporting Summary

Nature Research wishes to improve the reproducibility of the work that we publish. This form provides structure for consistency and transparency in reporting. For further information on Nature Research policies, see Authors & Referees and the Editorial Policy Checklist.

Statistical parameters

When statistical analyses are reported, confirm that the following items are present in the relevant location (e.g. figure legend, table legend, main text, or Methods section).

n/a	Confirmed	
☐	☒	The exact sample size (*n*) for each experimental group/condition, given as a discrete number and unit of measurement
☐	☒	An indication of whether measurements were taken from distinct samples or whether the same sample was measured repeatedly
☐	☒	The statistical test(s) used AND whether they are one- or two-sided *Only common tests should be described solely by name; describe more complex techniques in the Methods section.*
☐	☒	A description of all covariates tested
☐	☒	A description of any assumptions or corrections, such as tests of normality and adjustment for multiple comparisons
☐	☒	A full description of the statistics including central tendency (e.g. means) or other basic estimates (e.g. regression coefficient) AND variation (e.g. standard deviation) or associated estimates of uncertainty (e.g. confidence intervals)
☐	☒	For null hypothesis testing, the test statistic (e.g. *F*, *t*, *r*) with confidence intervals, effect sizes, degrees of freedom and *P* value noted *Give P values as exact values whenever suitable.*
☒	☐	For Bayesian analysis, information on the choice of priors and Markov chain Monte Carlo settings
☒	☐	For hierarchical and complex designs, identification of the appropriate level for tests and full reporting of outcomes
☐	☒	Estimates of effect sizes (e.g. Cohen's *d*, Pearson's *r*), indicating how they were calculated
☐	☒	Clearly defined error bars *State explicitly what error bars represent (e.g. SD, SE, CI)*

Our web collection on statistics for biologists may be useful.

Software and code

Policy information about availability of computer code

Data collection	Electrophysiology data were collected and analyzed using IgorPro v.5.05A (see below). Calcium imaging data was collected on a two-photon microscope, but analyzed using a modified Python (on Jupyter 5.5) script. Confocal images were acquired using Zen 2011 v8.1.
Data analysis	Statistical tests were conducted using Prism v8.0 (GraphPad) software for most analyses. Bowtie 0.12.7, RSEM 1.2.19, Seurat R v2.0, and RStudio 1.0.136 was used for QC, analysis, and exploration of single cell RNA-seq data. Electrophysiology data were analyzed using a custom program written with Igor Pro v.5.05A software (Wavemetrics). Confocal microscopy image analysis was done using Fiji ImageJ v2.0. Calcium imaging was analyzed using a modified Python (on Jupyter 5.5) script (available on GitHub).

For manuscripts utilizing custom algorithms or software that are central to the research but not yet described in published literature, software must be made available to editors/reviewers upon request. We strongly encourage code deposition in a community repository (e.g. GitHub). See the Nature Research guidelines for submitting code & software for further information.

Data

Policy information about availability of data

All manuscripts must include a data availability statement. This statement should provide the following information, where applicable:

- Accession codes, unique identifiers, or web links for publicly available datasets
- A list of figures that have associated raw data
- A description of any restrictions on data availability

All unique materials such as patient-derived cell cultures are freely available and can be obtained by contacting the corresponding author and with a standard MTA with Stanford University. Single cell RNAseq data in Figure 1 was analyzed from publicly available datasets on GEO (Accession GSE89567 and GSE102130). Single cell RNAseq for Extended Data Figure 2 will be made accessible on GEO. Data for all figures can be found in manuscript, in accompanying source data, or from corresponding author upon reasonable request.

Field-specific reporting

Please select the best fit for your research. If you are not sure, read the appropriate sections before making your selection.

☒ Life sciences ☐ Behavioural & social sciences ☐ Ecological, evolutionary & environmental sciences

For a reference copy of the document with all sections, see nature.com/authors/policies/ReportingSummary-flat.pdf

Life sciences study design

All studies must disclose on these points even when the disclosure is negative.

Sample size	Based on the variance of xenograft growth in control mice, power calculations indicated use of at least 3 mice per genotype to give 80% power to detect an effect size of 20% with a significance level of 0.05. For electrophysiological studies, all studies were replicated across multiple cohorts of mice to verify reproducibility.
Data exclusions	No data were excluded from the analyses.
Replication	All attempts at replication were successful with biological replicates performed on separate cohorts of animals/cells.
Randomization	All animals xenografted with individual cell lines were analyzed in the same way - no randomization was necessary in the design of this study.
Blinding	The experimenter performing histological quantifications was blinded to group allocation.

Reporting for specific materials, systems and methods

Materials & experimental systems

n/a	Involved in the study
☐	☒ Unique biological materials
☐	☒ Antibodies
☐	☒ Eukaryotic cell lines
☒	☐ Palaeontology
☐	☒ Animals and other organisms
☐	☒ Human research participants

Methods

n/a	Involved in the study
☒	☐ ChIP-seq
☒	☐ Flow cytometry
☒	☐ MRI-based neuroimaging

Unique biological materials

Policy information about availability of materials

Obtaining unique materials	All unique materials such as patient-derived cell cultures are freely available and can be obtained by contacting the corresponding author and with a standard MTA with Stanford University.

Antibodies

Antibodies used	Primary antibodies used in immunohistochemistry: chicken anti-neurofilament-H (1:1000; #NFH Aves Labs; Lot#7857983),

chicken anti-neurofilament-M (1:1000; #NFM Aves Labs; Lot#1757985), guinea pig anti-synpasin1/2 (1:500; #106-004 Synaptic Systems), chicken anti-GFP (1:500; #Ab13970 Abcam; Lot#GR3190550-10), mouse anti-human nuclei clone 235-1(1:100; #MAB1281 Millipore; Lot#3189191), rabbit anti-Ki67 (1:500; #Ab15580 Abcam; Lot#GR3198167-1), rabbit anti-cleaved caspase 3 (1:200; #9661S Cell Signaling; Lot#43), mouse anti-MAP2 (1:1000; #MAB3418 Millipore; Lot#1993775), rabbit anti-histone H3.3 K27M mutant (1:500; #190631 Abcam; Lot#GR239194-7), mouse anti-nestin (1:500, #Ab6320 Abcam), rabbit anti-RFP (1:500; #600-401-379 Rockland; Lot#39707), or Streptavidin Alex Fluor 594 conjugate (1:500; #S32356 Thermo Fisher; Lot#1902487)

For secondary antibodies: Alexa 488 donkey anti-chicken IgG (#703-545-155; Lot#142355); Alexa 594 donkey anti-rabbit IgG (#711-585-152; Lot#140019), Alexa 647 donkey anti-mouse IgG (#715-605-150; Lot#139301), Alexa 405 donkey anti-guinea pig IgG (#706-475-148; Lot#140331), Alexa 647 donkey anti-rabbit IgG (#711-605-152; Lot#140551) , or Alexa 594 donkey anti-mouse IgG (#715-585-150; Lot#140149) all used at 1:500 (Jackson Immuno Research).

Validation

All antibodies have been validated in the literature and/or in Antibodypedia for use in mouse immunohistochemistry. To further validate the antibodies on our hands, we confirmed that each antibody stained in the expected cellular patterns and brain-wide distributions for immunohistochemistry. For the case of cleaved caspase-3 staining, we confirmed antibody staining in mouse brain tissue of a disease model as a positive control.

Eukaryotic cell lines

Policy information about cell lines

Cell line source(s)

The eukaryotic cell cultures used are patient-derived cultures of high-grade gliomas generated in the Monje lab from biopsy (SU-pcGBM2) or autopsy tissue (SU-DIPG-VI, SU-DIPGXIII-FL, SU-DIPG25). 293T cells (ATCC) were used only for virus production.

Authentication

Sort Tandem Repeat (STR) fingerprinting is performed every 3 months on all cell cultures to ensure authenticity.

Mycoplasma contamination

All cell cultures are routinely tested for mycoplasma contamination and all cultures used tested negative.

Commonly misidentified lines
(See ICLAC register)

No commonly misidentified lines were used.

Animals and other organisms

Policy information about studies involving animals; ARRIVE guidelines recommended for reporting animal research

Laboratory animals

Both male and female NOD-SCID-IL2R gamma chain-deficient (NSG) were used between 4-12 weeks of age.

Wild animals

No wild animals were used.

Field-collected samples

No field-collected samples were used.

Human research participants

Policy information about studies involving human research participants

Population characteristics

The three human subjects whose data was used in Figure 5 were all adult males diagnosed with IDH WT glioblastoma. Clinical information is available in Table 1.

Recruitment

All human electrocorticography data was obtained passively from adult patients undergoing intraoperative brain mapping for surgical resection by co-author S.H.J. Each individual was recruited from a prospective registry of adults aged 18–85 with newly diagnosed frontal, temporal, and parietal IDH-wild type WHO IV glioblastomas. Informed consent for this study was obtained in accordance with the University of California, San Francisco (UCSF) institutional review board for human research (UCSF CHR 17-23215). Subjects with tumors projecting to the cortical surface and at least three electrocorticography channels overlaying healthy-appearing brain (as determined by absence of FLAIR or T1 post gadolinium enhancement) were selected for analysis.